The Astrophysical Journal, 704:306–323, 2009 October 10 doi:10.1088/0004-637X/704/1/306

DUST AND THE TYPE II-PLATEAU SUPERNOVA 2004et

R. Kotak[1], W. P. S. Meikle[2], D. Farrah[3], C. L. Gerardy[4], R. J. Foley[5], S. D. Van Dyk[6], C. Fransson[7], P. Lundqvist[7], J. Sollerman[7,8], R. Fesen[9], A. V. Filippenko[5], S. Mattila[10], J. M. Silverman[5], A. C. Andersen[8], P. A. Höflich[4], M. Pozzo[11], and J. C. Wheeler[12]

[1] Astrophysics Research Centre, School of Mathematics and Physics, Queen's University Belfast, BT7 1NN, UK; r.kotak@qub.ac.uk
[2] Astrophysics Group, Blackett Laboratory, Imperial College London, Prince Consort Road, London SW7 2AZ, UK
[3] Astronomy Centre, Department of Physics and Astronomy, University of Sussex, Brighton BN1 9QH, UK
[4] Department of Physics, Florida State University, 315 Keen Building, Tallahassee, FL 32306-4350, USA
[5] Department of Astronomy, University of California, Berkeley, CA 94720-3411, USA
[6] Spitzer Science Center, 220-6 Caltech, Pasadena, CA 91125, USA
[7] Department of Astronomy, Stockholm University, AlbaNova, SE-10691 Stockholm, Sweden
[8] Dark Cosmology Centre, Niels Bohr Institute, University of Copenhagen, Juliane Maries Vej 30, 2100 Copenhagen Ø, Denmark
[9] Department of Physics and Astronomy, 6127 Wilder Laboratory, Dartmouth College, Hanover, NH 03755, USA
[10] Tuorla Observatory, Department of Physics and Astronomy, University of Turku, Väisäläntie 20, FI-21500 Piikkiö, Finland
[11] Department of Earth Sciences, University College London, London WC1E 6BT, UK
[12] Astronomy Department, University of Texas at Austin, Austin, TX 78712, USA
Received 2009 April 18; accepted 2009 August 26; published 2009 September 22

ABSTRACT

We present mid-infrared (MIR) observations of the Type II-plateau supernova (SN) 2004et, obtained with the *Spitzer Space Telescope* between 64 and 1406 days past explosion. Late-time optical spectra are also presented. For the period 300–795 days past explosion, we argue that the spectral energy distribution (SED) of SN 2004et comprises (1) a hot component due to emission from optically thick gas, as well as free–bound radiation; (2) a warm component due to newly formed, radioactively heated dust in the ejecta; and (3) a cold component due to an IR echo from the interstellar-medium dust of the host galaxy, NGC 6946. There may also have been a small contribution to the IR SED due to free–free emission from ionized gas in the ejecta. We reveal the first-ever spectroscopic evidence for silicate dust formed in the ejecta of a supernova. This is supported by our detection of a large, but progressively declining, mass of SiO. However, we conclude that the mass of directly detected ejecta dust grew to no more than a few times $10^{-4}\,M_{\odot}$. We also provide evidence that the ejecta dust formed in comoving clumps of fixed size. We argue that, after about two years past explosion, the appearance of wide, box-shaped optical line profiles was due to the impact of the ejecta on the progenitor circumstellar medium and that the subsequent formation of a cool, dense shell was responsible for a later rise in the MIR flux. This study demonstrates the rich, multifaceted ways in which a typical core-collapse supernova and its progenitor can produce and/or interact with dust grains. The work presented here adds to the growing number of studies that do not support the contention that SNe are responsible for the large mass of observed dust in high-redshift galaxies.

Key words: circumstellar matter – dust, extinction – supernovae: general – supernovae: individual (SN 2004et)

Online-only material: color figures

1. INTRODUCTION

Historically, the opening up of the electromagnetic spectrum beyond the narrow visible region has always led to a deeper understanding of physical phenomena. Nowhere is this currently more evident than in the mid-infrared (MIR) regime where the combination of vastly superior sensitivity and spatial resolution afforded by the *Spitzer Space Telescope* (Werner et al. 2004), compared with previous infrared (IR) satellites, has transformed the study of extragalactic point sources.

Ground-based MIR studies of supernovae (SNe) are extremely challenging—if not impossible—even from the highest-altitude facilities. This is due to a combination of conspiring factors: strong terrestrial atmospheric absorption, generally high background in the MIR, and the faintness of MIR emission from SNe at epochs of interest.

Currently, one of the most persistent questions relating to SN research is whether core-collapse SNe could be major contributors to the universal dust budget. Although this was suggested about 40 years ago (Cernuschi et al. 1967; Hoyle & Wickramasinghe 1970), attempts to verify this hypothesis observationally have, until recently, remained few and far between. This has been partly due to a lack of sufficiently sensitive instrumentation, and partly because, given the large amounts of dust produced in the winds of low-mass stars in the local Universe, the notion that SNe might produce significant dust was not widely explored. However, the evidence in favor of enormous amounts of dust ($\gtrsim 10^8\,M_{\odot}$) in galaxies at high redshifts ($z \gtrsim 6$) is mounting, and comes from a variety of observations such as submillimeter observations of the most distant quasars (Bertoldi et al. 2003), obscuration by dust of quasars in damped Ly-α systems (DLAs; Pei et al. 1991), and measurements of metal abundances in DLAs (Pettini et al. 1997). The existence of large amounts of dust when the Universe was relatively youthful poses problems for a low-mass star origin of dust, since the main-sequence evolution timescales of these stars (up to 1 Gyr) begin to become comparable to the age of the Universe. SNe arising from short-lived population III stars could be a viable alternative. Although estimates of the amount of dust produced per supernova are sensitive to the choice of initial mass function and grain destruction efficiencies, the current consensus is that each SN needs only to produce 0.1–1 $M_{\odot}$ of dust to account for the high-redshift observations (Dwek et al. 2007; Meikle et al. 2007). However, for the

handful of recent SNe for which dust-mass estimates exist, these invariably fall short of the amounts cited above by 2–3 orders of magnitude.

There are at least two direct methods for inferring the presence of dust in the ejecta of recent SNe. The first relies on the attenuation of the red wings of optical or near-infrared (NIR) ejecta lines during the nebular phase, betraying the presence of new dust that has condensed in the ejecta. The signature is usually pronounced, and has not yet been attributed to any other effect. While this method has been used to infer the presence of freshly formed dust, quantitative information on the amount, composition, and geometry has remained elusive. The other method is to observe the thermal emission from dust grains. Although over a dozen SNe have exhibited NIR excesses, the challenge so far has been to distinguish between preexisting circumstellar dust heated by the SN and new dust condensing in the ejecta. The former scenario (i.e., the IR echo) predicts a distinctive flat-topped light-curve shape (e.g., Bode & Evans 1980; Dwek 1983), thus providing one means by which to differentiate between the two cases. The ideal observational requirement for this method to work is that of a long time series of MIR data. Additionally, multiwavelength MIR data provide information on the evolution of the spectral energy distribution (SED), thereby constraining the dust temperature, emissivity, and geometry.

In the case of SN 1987A, both techniques were employed. However, even the highest value obtained was only $7.5 \times 10^{-4}\ M_{\odot}$ (Ercolano et al. 2007). Pozzo et al. (2004) used the attenuation method to infer a dust mass exceeding $2 \times 10^{-3}\ M_{\odot}$ in the Type IIn SN 1998S. However, such events are relatively rare. For the Type II-plateau (II-P) supernova SN 1999em, Elmhamdi et al. (2003) used the attenuation method to obtain a lower limit to the dust mass of just $\sim 10^{-4}\ M_{\odot}$. More recently, using *Spitzer* observations, the thermal-emission approach has been applied to the Type II SN 2003gd. Meikle et al. (2007) found that the MIR flux at about 16 months was consistent with emission from just $4 \times 10^{-5}\ M_{\odot}$ of newly condensed dust in the ejecta. They also showed that the claim by Sugerman et al. (2006) of a much larger mass of new dust at a later epoch was unsupported by the data.

Evidence for dust condensation in SN ejecta may also be acquired via the study of supernova remnants (SNRs). However, MIR and far-IR (FIR) studies of SNRs have tended to find low dust masses. For example, for the Cassiopeia A SNR, Hines et al. (2004) used *Spitzer* images at 24 μm and 70 μm together with other data to deduce a dust mass of $3 \times 10^{-3}\ M_{\odot}$ at around 80 K in Cas A. From *Spitzer* spectroscopy, Rho et al. (2008) deduce a factor of 10 larger dust mass and suggest that the difference is due to their use of additional grain compositions necessary to fit the spectra. Three studies based on *Spitzer* data of the young SNR 1E 0102.2–7219 reveal dust masses that vary by roughly two orders of magnitude: Stanimirovic et al (2005) find no more than $8 \times 10^{-4}\ M_{\odot}$ of dust at $\sim$120 K associated with the remnant, while Sandstrom et al. (2009) and Rho et al. (2009) derive dust masses of $3 \times 10^{-3}\ M_{\odot}$ at about 70 K, and $10^{-2}\ M_{\odot}$ of dust at $\sim$60 K, respectively. Estimates for the Crab and Kepler's SNRs based on *Spitzer* MIR data are similar, with 10^{-3} to $10^{-2}\ M_{\odot}$ of dust for the former by Temim et al. (2006), and $3 \times 10^{-3}\ M_{\odot}$ at $\sim$85 K for the latter by Blair et al. (2007). Thus, the bulk of MIR/FIR studies of SNRs yield dust masses that are at least a factor of 10 less than the *minimum* required to account for the high-redshift dust.

It is possible that most of the SNR dust is very cold ($\lesssim$30 K) and hence has escaped detection in these studies. Attempts have been made to detect very cold dust using submillimeter measurements of the Cas A and Kepler SNRs. Observations by Dunne et al. (2003) using *SCUBA* led them to claim that at least $2\ M_{\odot}$ of dust formed in the supernova, with their model including a dust component at 18 K. However, Krause et al. (2004) used the same data together with observations from *Spitzer* to show that most of the emission originates from a line-of-sight molecular cloud, and not from dust formed in Cas A. Nevertheless, in a recent study of 850 μm polarization in Cas A, Dunne et al. (2009) still estimate a dust mass of $\sim 1\ M_{\odot}$. However, this estimate is subject to significant uncertainties in 850 μm emissivity as well as in grain alignment and morphology. In particular, they point out that iron (Dwek 2004) or graphite needles could reduce the dust mass required to explain the submillimeter observations. For the Kepler SNR, Morgan & Edmunds (2003) used *SCUBA* to infer a dust mass of $\sim 1\ M_{\odot}$, where the model fit included a dust component at 17 K. However, they subsequently revised this dust mass downward by a factor of two in the submillimeter study of Gomez et al. (2009). We conclude that, so far, the direct submillimeter evidence in favor of large masses of ejecta dust is relatively weak. On the other hand, several studies have highlighted the destruction of dust grains by the reverse shock as the supernova ejecta crashes into the ambient medium and makes the transition into the remnant phase (e.g., Williams et al. 2006; Nozawa et al. 2007). This implies that the dust masses that condense in SN ejecta at early epochs (few years) should be several times higher than during the remnant phase.

All of the above findings have rekindled the debate regarding the role of SNe as dust producers, and vigorous efforts are underway to address this question.

Spitzer's coverage of the likely peak of thermal emission due to dust, together with the availability of flexible scheduling of observations, provided an opportunity to test the SN ejecta dust-condensation hypothesis, at least for local supernovae. We have therefore been pursuing a campaign of MIR observations for a sample of core-collapse SNe within the framework of the Mid-Infrared Supernova Consortium (MISC).

Fortuitously, there have been several nearby supernovae since the launch of *Spitzer* in 2003, which have also been well monitored at other wavelengths. In Kotak et al. (2005), we reported early results on SN 2004dj, the first MIR observations of SN ejecta since those of SN 1987A. *Spitzer* studies by Barlow et al. (2005) and Meikle et al. (2006) of the Type II-P SN 2002hh revealed the complicated nature of its surroundings. However, both sets of authors concluded that the MIR flux from this SN was dominated by emission from a dusty circumstellar medium (CSM) or nearby molecular cloud, driven by the SN luminosity. This radiation swamped any prospects of detecting newly formed ejecta dust in this case.

In what follows we present the most extensive MIR data set of any SN to date, surpassed only in the timespan of observations by the Type II-pec SN 1987A, which has been observed at MIR wavelengths as late as 18 years after explosion (Bouchet et al. 2006). Moreover, it can be argued that since SN 2004et is of Type II-P, the most common of all core-collapse SN types, the MIR work presented here is of particular relevance to the general understanding of the role played by SNe in the formation of dust grains.

1.1. SN 2004et

SN 2004et was discovered on 2004 September 22.98 (UT dates are used throughout this paper) by S. Moretti (Zwitter & Munari 2004) and is the eighth supernova to occur in NGC 6946 since 1917. Following Li et al. (2005), we adopt an explosion date (epoch 0 days) of 2004 September 22.0 (MJD = JD-2400000.5 = 53270.0). The distance to NGC 6946 has been estimated using several different techniques. However, as pointed out by Li et al. (2005), the uncertainty is large. For consistency with our earlier work on SN 2002hh in the same host galaxy (Meikle et al. 2006) a distance of 5.9 Mpc is adopted (Karachentsev et al. 2000). Soon after discovery, the SN was spectrally classified as a young Type II-P SN, exhibiting characteristic broad P Cygni profiles in the Balmer lines (Zwitter et al. 2004; Filippenko et al. 2004). Photometric and spectroscopic monitoring programs began in earnest soon thereafter. Results from optical monitoring are summarized by Sahu et al. (2006) and Misra et al. (2007).

Based on pre-explosion imaging, Li et al. (2005) suggested a yellow supergiant as a candidate progenitor for SN 2004et. This has since been challenged by R. M. Crockett et al. (2009, in preparation), who show that the point source seen in ground-based images comprises at least three separate sources. They argue that the true progenitor is actually an M-type red supergiant. X-ray (Rho et al. 2007) and radio (Martí-Vidal et al. 2007) observations at early times have revealed the presence of a progenitor wind rendered detectable through the impact of the fastest-moving ejecta.

2. MID-INFRARED OBSERVATIONS OF SN 2004et

SN 2004et was observed using the full suite of *Spitzer* instrumentation. Images at 3.6, 4.5, 5.8, and 8.0 μm were obtained with the Infrared Array Camera (IRAC), at 16 and 22 μm with the Infrared Spectrograph (IRS) Peak-up Array (PUI), and at 24 μm with the Multiband Imaging Photometer for Spitzer (MIPS). Spectra between 5.2 and 37 μm were acquired with the IRS in a low-resolution mode. Imaging observations spanned epochs 64.7–1406.0 days. These observations were drawn from a number of programs in addition to our own, and are catalogued in Table 1. Several pre- and post-explosion 3.6 μm IRAC images are shown in Figure 1.

2.1. Mid-Infrared Photometry of SN 2004et

We used the post-basic calibrated data (PBCD) products provided by the *Spitzer* pipeline. The serendipitous pre-explosion IRAC and MIPS images from the SINGS program showed evidence for spatially extended emission at and near the location of the supernova. We therefore subtracted these "templates" from all epochs of post-explosion imaging before proceeding with our flux measurements. The image matching and subtraction was performed as implemented in the ISIS v2.2 image-subtraction package (Alard & Lupton 1998; Alard 2000), and modified in a manner analogous to that described by Meikle et al. (2006).

Aperture photometry was performed on the background-subtracted IRAC and MIPS images using the Starlink package GAIA (Draper et al. 2002). A circular aperture of radius 5″ was used for the photometry. This was chosen as a compromise between minimizing the effects of the residual ridge emission at the SN location at late epochs in the IRAC and MIPS data and minimizing the size of aperture correction needed in the final flux determination. The aperture radius corresponds to a distance of ∼145 pc at SN 2004et. Residual background in the template-subtracted IRAC and MIPS images was measured and subtracted by using a clipped mean sky estimator and a concentric sky annulus having inner and outer radii of 1.5 and 2 times the aperture radius, respectively. Aperture corrections were derived from the IRAC and MIPS point-response function frames available from the Spitzer Science Center, and ranged from a factor of 1.08 at 3.6 μm to a factor of 2.12 at 24 μm. Fluxing errors due to uncertainties in the aperture corrections are about ±5%. At earlier epochs the aperture was centered by centroiding on the SN image. At later epochs, when the supernova was faint, the aperture was centered using the WCS coordinates, with the SN position given by the radio observation of Stockdale et al. (2004).

For the PUI images (16 and 22 μm), no pre-explosion data were available. We carried out standard aperture photometry on the PBCD images using the same sizes of aperture and annulus as for the IRAC and MIPS measurements. The residual background was then estimated as follows. Using the same aperture and sky annulus, we measured the net fluxes at the SN location in the pre-explosion IRAC and MIPS images (see Table 1). The residual background at 16 and 22 μm was then found by blackbody interpolation between the IRAC and MIPS wavelengths and subtracted from the previously measured PUI fluxes. The resulting SN photometric measurements are listed in Table 1 and displayed as light curves in Figure 2. The uncertainties shown are statistical only.

2.2. Mid-Infrared Spectroscopy of SN 2004et

Low-resolution ($R \approx 60$–127) MIR spectroscopy of SN 2004et covered seven epochs between 294 and 1385 days and was obtained using the short–low (SL; 5.2–14.5 μm) and long–low (LL; 14–38 μm) modules of the Infrared Spectrograph (IRS; Houck et al. 2004). The log of observations is given in Table 2.

We began our reduction of the SL and LL spectra with the basic calibrated data (BCD) frames. Starting with these frames, we first subtracted the sky background by differencing between the two nod positions. All subsequent steps (extraction, wavelength calibration, and flux calibration) were carried out using the optimal extraction mode of the *Spitzer* Custom Extractor tool, SPICE. Given the faintness of the target by day 1212, we also experimented with subtracting the sky background by differencing between the adjacent order and carrying out subsequent extraction steps using the Spectroscopic Modeling, Analysis, and Reduction Tool (SMART). We found the two extractions to be consistent but with the latter producing a cleaner spectrum, so we used this extraction. A possible reason for this difference may be that order–order sky subtraction is more suited for removing background emission when the background is high and variable (see below).

Despite this careful reduction procedure, the fluxes of the IRS spectra and the IRAC photometry were not completely consistent. The main problem was that the SN lay on a ridge of emission in the host galaxy (Figure 1(a)). While this could be removed for the IRAC and MIPS images using the template method described above, such a technique was not possible for the spectra. Furthermore, this problem was aggravated by differences in the fixed sizes of the spectrograph aperture slits and the circular apertures used for the image photometry. An additional, though smaller, problem was that the spectra were generally taken a few days before or after the images, during which time the SN flux changed.

In order to correct for these difficulties, we calibrated the IRS spectra against nearly contemporary photometry in the 8 μm

Table 1
Background-Subtracted Mid-IR Photometry of SN 2004et

Date	MJD	Epoch[†]	t_{exp}	Flux (μJy)						
		(d)	(s)	IRAC				PUI		MIPS
				3.6 μm	4.5 μm	5.8 μm	8.0 μm	16 μm	22 μm	24 μm
2004 Jun 10[a]	53166.8	−103.2	107	84.9(4.1)	47.5(4.9)	165(17)	351(45)	...	...	...
2004 Jul 9[a]	53196.0	−74.0	81	...	...	...	...	...	...	268(46)
2004 Jul 11[a]	53197.2	−72.8	81	...	...	...	...	...	...	207(37)
2004 Nov 25[a]	53334.7	64.7	107	17020(30)	13200(20)	9490(30)	5950(30)	...	...	...
2005 Jul 13[b]	53564.9	294.9	629	...	...	...	...	676(49)	...	...
2005 Jul 19[c]	53570.9	300.9	14	686(17)	2994(20)	1344(50)	2277(40)	...	...	...
2005 Jul 20[b]	53571.2	301.2	536	697(3)	3040(5)	1446(13)	2252(29)	...	...	...
2005 Aug 3[c]	53585.5	315.5	159	...	...	...	...	...	...	670(50)
2005 Sep 17[c]	53630.8	360.8	14	475(12)	1725(20)	1064(48)	1930(55)	...	...	...
2005 Sep 24[c]	53637.0	367.0	159	...	...	...	...	...	...	685(45)
2005 Nov 2[b]	53676.0	406.0	536	319(3)	1148(3)	706(13)	1600(25)	...	...	...
2005 Dec 22[b]	53726.5	456.5	629	...	...	...	...	657(45)	...	...
2005 Dec 30[c]	53734.9	464.9	14	193(15)	640(19)	540(70)	1224(43)	...	...	...
2006 Jan 10[c]	53745.7	475.7	159	...	...	...	...	...	...	667(65)
2006 Aug 4[d]	53951.3	681.3	315	...	...	...	...	434(48)	791(50)	...
2006 Aug 13[e]	53960.5	690.5	29	<35 (2σ)	33(15)	150(60)	430(30)	...	...	...
2006 Sep 1[e]	53979.2	709.2	159	...	...	...	...	...	...	480(65)
2006 Sep 10[e]	53988.9	718.9	57	...	...	...	...	296(47)	...	...
2006 Sep 28[d]	54006.2	736.2	268	15(5)	52(3)	<67 (2σ)	248(18)	...	...	...
2006 Oct 18[d]	54026.5	756.5	629	...	...	...	...	416(46)	742(55)	...
2006 Nov 26[d]	54065.9	795.9	536	<5 (2σ)	22(3)	<40 (2σ)	172(19)	...	...	...
2006 Dec 29[e]	54098.0	828.0	250	<5 (2σ)	38(3)	<35 (2σ)	65(32)*	...	...	...
2007 Jan 21[e]	54121.2	851.2	494	...	...	...	...	...	...	600(65)
2007 Jan 27[e]	54127.5	857.5	132	...	...	...	...	251(48)	...	...
2007 Jun 26[e]	54277.1	1007.1	283	...	...	...	...	100(48)	...	...
2007 Jul 4[e]	54285.0	1015.0	283	<3 (2σ)	20.7(2.8)	<30 (2σ)	109(19)	...	...	...
2007 Jul 10[e]	54291.1	1021.1	494	...	...	...	...	...	...	511(59)
2007 Aug 2[f]	54314.3	1044.3	283	...	...	...	...	149(45)	...	...
2007 Aug 12[f]	54324.4	1054.4	322	<4 (2σ)	16.2(2.5)	<30 (2σ)	134(35)	...	...	...
2007 Aug 27[g]	54339.7	1069.7	93	...	...	...	...	...	...	554(30)
2007 Aug 27[f]	54339.7	1069.7	494	...	...	...	...	...	...	480(35)
2007 Oct 12[g]	54385.2	1115.2	1258	...	...	...	...	956(54)	...	...
2007 Oct 22[g]	54395.9	1125.9	3485	66.4(1.5)	189.9(2.6)	335(9)	373(31)	...	...	...
2007 Dec 27[f]	54461.1	1191.1	322	52.2(2.1)	197.0(2.8)	320(12)	444(37)	...	...	...
2008 Jan 07[f]	54472.5	1202.5	494	...	...	...	...	...	...	1192(74)
2008 Jan 17[g]	54482.2	1212.2	1258	...	...	...	...	962(45)	...	...
2008 Jan 27[g]	54492.8	1222.8	536	53.8(1.2)	219(3)	360(14)	335(25)	...	...	...
2008 Feb 14[g]	54510.6	1240.6	93	...	...	...	...	...	...	1195(55)
2008 Jul 18[f]	54665.8	1395.8	322	85.7(1.5)	270(2)	456(8)	633(23)	...	...	...
2008 Jul 29[f]	54676.0	1406.0	494	...	...	...	...	...	...	1461(26)
Background	...	...	...	84.9(4.1)	47.5(4.9)	165(17)	351(45)	345(40)**	250(40)**	238(30)

Notes. Statistical uncertainties in the last one or two significant figures are shown in parentheses. [†] Following Li et al. (2005), we assume an explosion date of 2004 September 22.0 (MJD = 53270.0).

[a] PID. 00159 Kennicutt et al. (SINGS). [b] PID. 20256 Meikle et al. (MISC). [c] PID. 20320 Sugerman et al. (SEEDS). [d] PID. 30292 Meikle et al. (MISC). [e] PID. 30494 Sugerman et al. (SEEDS). [f] PID. 40010 Meixner et al. (SEEDS). [g] PID. 40619 Kotak et al. (MISC).

* Owing to the weakness of the 8 μm flux at this epoch and the consequent difficulty of correcting for the strong, complex background via the usual annular sky measurement, the background was, instead, measured using five 5″-radius apertures around the target aperture. This allowed the exclusion of the worst irregularity in the residual background.

** No pre-explosion PUI data available. Background estimated by blackbody interpolation between pre-explosion IRAC and MIPS photometry.

band, chosen since it was completely spanned by the short–low (SL) spectrum. The IRAC 8 μm transmission function was multiplied by the MIR spectra and by a model spectrum of Vega. The resulting MIR spectra for the SN and Vega were integrated over wavelength and compared. Hence, the total SN spectral fluxes in the 8 μm band were derived. These were then compared with the temporally nearest 8 μm photometry to derive scaling factors by which the spectra were multiplied. Correction factors were, respectively, $\times$0.82, $\times$0.84, $\times$0.75, $\times$0.76, $\times$0.37, $\times$1.0, and $\times$0.94 for SL spectra at 294, 349, 450, 481, 823, 1212, and 1385 days, respectively. The IRAC photometry epochs to which these spectra were scaled were 300, 360, 464, 464, 795, 1222, and 1395 days, respectively.

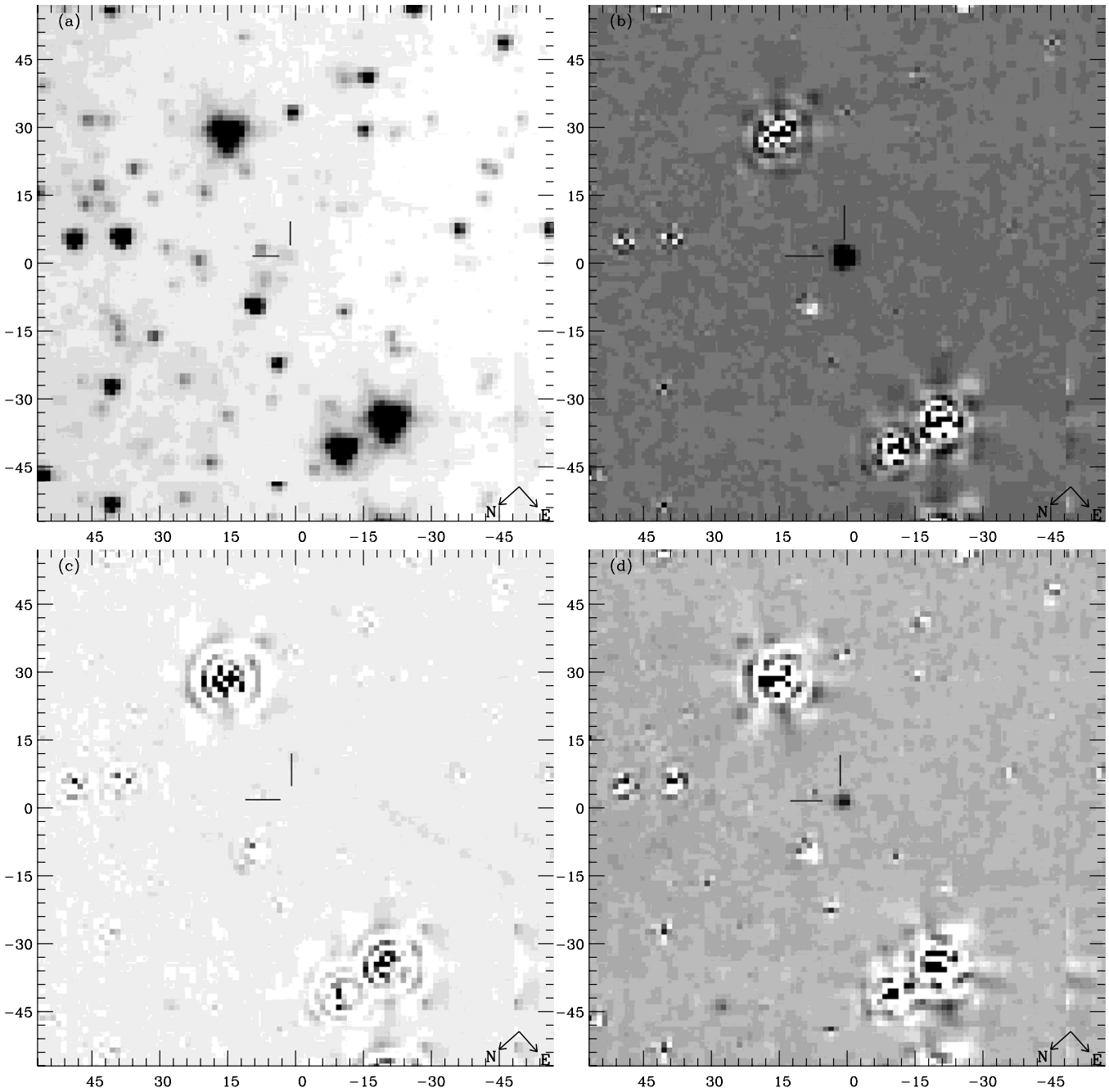

Figure 1. Subsections of the immediate field around SN 2004et at 3.6 μm. Both axes are given in arcsec, and the field is only approximately centered on the supernova. Panel (a) shows the pre-explosion image, while panels (b), (c), and (d) show template-subtracted frames of the same field at 300, 795, and 1222 days, respectively, revealing the dramatic changes in brightness over this timespan (see also Table 1). Short dashes mark the position of the SN ($\alpha_{J2000} = 20^h35^m25\overset{s}{.}33$; $\delta_{J2000} = +60°07'17\overset{''}{.}7$), which lies $247\overset{''}{.}1$ E and $115\overset{''}{.}4$ S of the galaxy nucleus.

The bulk of the corrections was due to errors in the original spectral flux calibration. Apart from the 823 day spectrum,[13] only a small part of these corrections was due to the shift from the spectral epochs to the contemporary photometry epochs. The large correction at day 823 may have been due to the faint SN flux around this time and the consequent strong effect of the residual ridge emission. We did not detect the source in SL order 2 on day 1212, so the spectrum only covered about 2/3 of the 8 μm IRAC band. Within this restriction, we found that the spectrum provided a match to the 1222 day photometry without any scaling.

For five of the spectral epochs (294, 349, 450, 1212, and 1385 days), usable contemporary LL spectra, typically spanning ~14–30 μm, were also available. The first three had a small overlap with the SL spectra in the 14 μm region. These were scaled to bring them into agreement with the SL spectra in this region. The LL correction factors were, respectively, ×0.7, ×0.5, and ×0.45. No SL–LL overlap was available for spectral epochs 1212 and 1385 days. Instead, theses spectra were compared with contemporary 24 μm fluxes obtained with MIPS.

[13] The most contemporary set of IRAC data to the day 823 spectrum was actually obtained only five days later on day 828. However, owing to the weakness of the day 828 8 μm flux and the consequent difficulty of reliably correcting for the strong, complex background even after template subtraction, we decided to scale the day 823 spectrum to day 795 when the SN was considerably brighter.

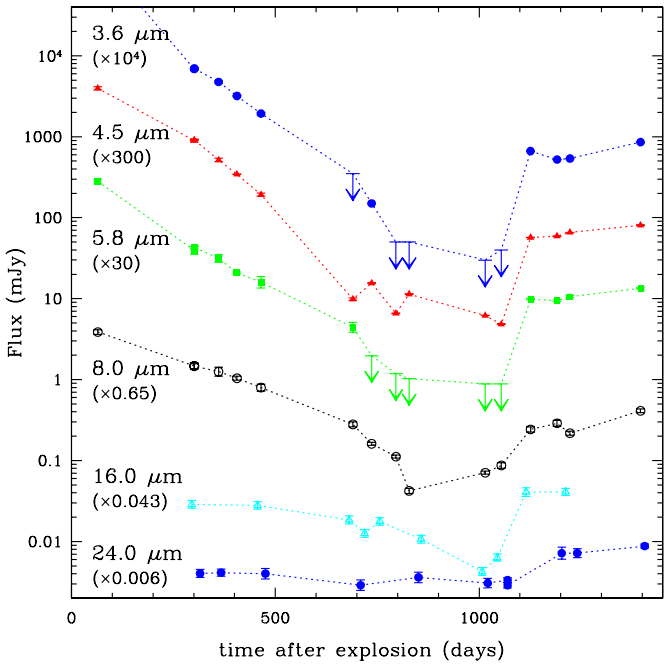

Figure 2. Mid-infrared template-subtracted light curves of SN 2004et. The upper limits are at 2σ. For clarity the light curves have been shifted vertically by the factors shown in parentheses.

(A color version of this figure is available in the online journal.)

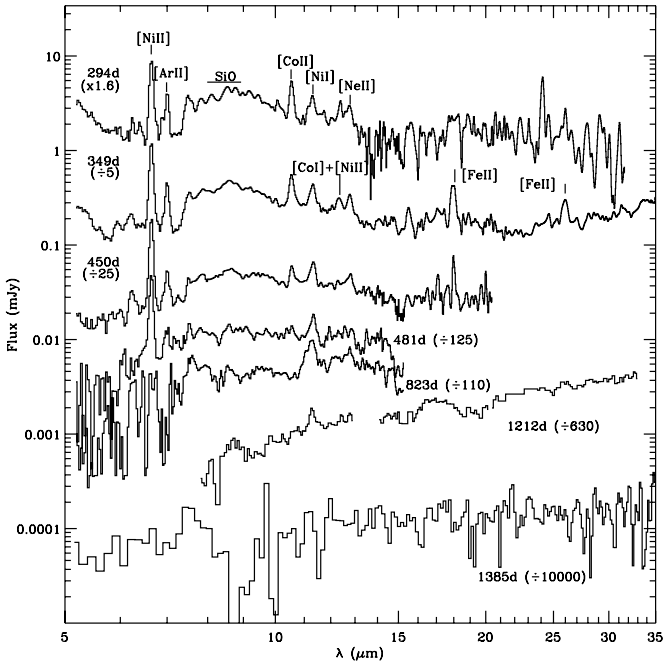

Figure 3. MIR spectra of SN 2004et. While the epochs shown in the diagram correspond to the original spectroscopic ones, the respective spectra have been scaled to match contemporary IRAC epochs at (respectively) 300, 360, 464, 464, 795, 1222, and 1395 days (see Section 2.2). For clarity, the spectra have been shifted vertically by the amounts shown in parentheses.

Table 2
Mid-IR Spectroscopy of SN 2004et

Date (UT)	MJD	Epoch† (d)	Spectral range 5.2–8.7 μm	7.4–14.5 μm	14.0–21.3 μm	19.6–35 μm
2005 Jul 13[a]	53564.87	294.9	x	x	x	x
2005 Sep 06[b]	53619.77	349.8	x	x	x	x
2005 Dec 16[b]	53720.77	450.8	x	x	x	...
2006 Jan 16[a]	53751.01	481.0	x	x	x††	x††
2006 Dec 24[c]	54093.12	823.1	x	x	...	...
2008 Jan 17[d]	54482.20	1212.2	x	x	x	x
2008 Jul 8[e]	54655.60	1385.6	x	x	x	x

Notes. Spectral ranges observed at each epoch are indicated by "x." These correspond to the SL first and second orders (7.4–14.5 and 5.2–8.7 μm, respectively) and the LL first and second orders (19.6–38 and 14.0–21.3 μm, respectively).

† Following Li et al. (2005), we assume an explosion date of 2004 September 22.0 (MJD = 53270.0).

†† The LL spectra from day 481 were of low S/N and contaminated by residual background. They are not shown in Figure 3 nor used in the analysis.

[a] PID. 20320 Sugerman et al. (SEEDS). [b] PID. 20256 Meikle et al. (MISC). [c] PID. 30292 Meikle et al. (MISC). [d] PID. 40619 Kotak et al. (MISC). [e] PID. 40010 Meixner et al. (SEEDS).

For day 1212 the 14–21.3 μm portion required no correction to provide a match to the photometry. The 19.6–35 μm portion was scaled by a factor of 0.75 to match the overlap with the shorter wavelength section. For day 1385 the LL portion was scaled by ×0.63 to match the contemporary photometry. The spectra are plotted in Figure 3. Note that, while the epoch labels shown in Figure 3 correspond to the original spectroscopic ones, the respective spectra have been scaled, via the above procedure, to match the contemporary photometry. These corrections are important for the analysis below, which makes use of both the spectra and the photometry. The day 481 spectrum was not used in the analysis below. This was because of (1) the lack of a usable LL component, and (2) the close temporal proximity of the day 481 SL spectrum to that on day 450.

2.3. Very Late-time Optical Spectroscopy of SN 2004et

Optical spectra (∼4000–9000 Å) were taken using the Low-Resolution Imaging Spectrometer (LRIS; Oke et al. 1995) mounted on the Keck I 10 m telescope on 2006 December 25 and 2007 November 12 (days 823 and 1146, respectively) and the Deep Imaging Multi-Object Spectrograph (DEIMOS; Faber et al. 2003) mounted on the Keck II 10 m telescope on 2007 April 14 (day 933). We used a 1.″0 wide slit which was aligned along the parallactic angle to reduce differential light losses (Filippenko 1982). All spectra were reduced using standard techniques with CCD processing and optimal extraction for the LRIS data using IRAF. We obtained the wavelength scale from low-order polynomial fits to calibration-lamp spectra. Small wavelength shifts were then applied to the data after cross-correlating a template sky spectrum to the night-sky lines that were extracted with the SN. Using our own IDL routines, we fit spectrophotometric standard-star spectra to the data in order to flux calibrate our spectra and remove telluric lines (Wade & Horne 1988).

Due to the faintness of the supernova ($V \approx 22$ mag) the signal-to-noise ratio (S/N) is generally low. Spectra in the 5800–8000 Å region are shown in Figure 4, binned to a pixel width of 4 Å (∼180 km s^{-1}), and compared with spectra obtained by Sahu et al. (2006) on days 300 and 465. The characteristic ejecta Hα emission profile seen in the Sahu et al. (2006) spectra may be still apparent at 823 and 933 days, with a half-width at zero intensity (HWZI) of ∼2000 km s^{-1}. Its presence at 1146 days is less certain. However, on days 823, 933, and 1146 a wide, steep-sided, box-like ("square") component with HWZI = 8500 km s^{-1} is also present. Given the large decline in the SN flux between day 465 and 823, it is difficult to determine when the wide component actually appeared. A similar broadening of the

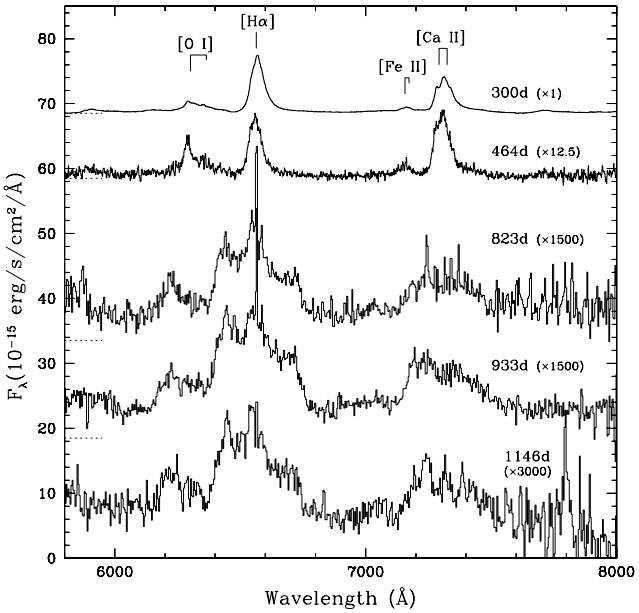

Figure 4. Late-time optical spectra of SN 2004et. The earlier two are from Sahu et al. (2006) (via the SUSPECT database). The later three are from the Keck telescopes. The approximate fluxes from two faint stars lying within the seeing disk have been subtracted from the Keck spectra (see text). All the spectra have been scaled by the amounts shown in parentheses. In addition, the upper-four spectra have been shifted vertically for clarity. The horizontal dotted lines indicate the zero-flux levels for these spectra.

[Ca II] feature at 7300 Å can be seen. The [O I] λλ6300, 6364 line shows a shift to the blue of ∼3000 km s^{-1}. We believe that this is due to the same "box-like profile" phenomenon as seen in the Hα and [Ca II] lines. However, as the [O I] line is weaker and close to Hα, we only see the stronger blue wing.

Superimposed on the box-like profile of Hα is a narrow component that is clearly visible in all three Keck spectra. In the highest resolution spectrum (day 933), the line is barely resolved at a resolution of about 1.5 Å (70 km s^{-1}). However, the profile does appear asymmetric, with a blue wing extending to about 3 Å (140 km s^{-1}) from the line peak. Narrow [N II] λλ6548, 6583 emission is also clearly visible, especially in the day 823 spectrum; a feature at 6717 Å due to [S II] may also be present, although the corresponding [S II] λ6731 line and the [O III] λλ4959, 5007 lines are absent.

The presence of this narrow feature is intriguing. While we cannot conclusively rule out a line-of-sight H II region as being responsible for the narrow emission, we note that the feature is not inconsistent with flash-ionized, undisturbed circumstellar material resulting from the progenitor wind. Also, between days 823 and 933, this component shifts by +90 km s^{-1}; currently, we have no explanation for this behavior, but note that it is not due to an error in the wavelength calibration that was cross-checked with respect to the night-sky lines (see above). Furthermore, there is no report of any narrow features in a high-resolution echelle spectrum taken about a week after discovery (Zwitter et al. 2004).

We defer further discussion of the circumstellar interaction to Section 3.2.2.

3. ANALYSIS

3.1. Evidence for Dust

The evolution of the MIR spectral continuum and the SED point strongly to IR emission from dust playing a significant and increasing role in the overall flux distribution of SN 2004et. To explore this proposition further, we make use of the MIR photometry (see Table 1) and spectra (Figure 3), together with optical photometry (Sahu et al. 2006; Misra et al. 2007) and spectra (Sahu et al. 2006).[14] In addition, for the period 823–1146 days, we derived approximate optical magnitudes from the Keck spectra and from the study of R. M. Crockett et al. (2009, in preparation), as follows.

R. M. Crockett et al. (2009, in preparation) report *Hubble Space Telescope (HST)* WFPC2 and NICMOS photometry of the SN 2004et field, using observations on day 1019 from program GO-11229 (PI: Meixner). These show that the single point source at the SN location seen in ground-based images resolves into three point sources. The brightest of these lies at the SN position, and we assume that this source is, or at least contains, the actual SN. They provide WFPC2 and NICMOS magnitudes for the three sources. We have made use of these results to correct for the flux of the two non-SN sources in the 823–1146 day optical data. To convert to *BVRI* magnitudes, we first matched a double blackbody to the combined fluxes of the non-SN sources. The resulting function was multiplied by typical *BVRI* transmission functions and then compared with a similarly processed model spectrum of Vega. The *BVRI* magnitudes for the *HST* SN source (day 1019) were obtained similarly, using a single blackbody match. We estimate an uncertainty of ±0.1 mag in the values derived by these procedures. The *HST*-based magnitudes are shown in Table 3.

R. M. Crockett et al. (2009, in preparation) also report ground-based *BVRI* photometry of SN 2004et on day 1054, obtained using the William Herschel Telescope (WHT) AUX imager. We corrected these data for the two nearby non-SN sources, and the net magnitudes are given in Table 3.

To derive *BVRI* magnitudes from the Keck spectra, the non-SN double-blackbody was first subtracted from each spectrum. The net spectra were then multiplied by *BVRI* filter transmission functions and compared with a similarly processed model spectrum of Vega. The values obtained are given in Table 3. (There is no *B* value on day 933 since at this epoch there was only partial coverage of the relevant part of the spectrum.) Given the difficult observing conditions, we estimate that the magnitudes based on the Keck spectra have a precision of ∼±0.2 mag.

In Figure 5, we show the later parts of the Sahu et al. (2006) light curves together with the 823–1146 day magnitudes described above, all corrected for the fluxes from the two faint nearby stars. The light curves appear to reach a minimum around ∼1000 days and then begin to rise again. Similar behavior is seen in the MIR light curves (Figure 2); see also the 4.5 μm light curve plotted in Figure 5 for comparison. This will be discussed later.

To take an initially neutral standpoint on the interpretation, we compared blackbodies with the data, scaled to the IRAC epochs. The MIR spectra were scaled as explained above. In addition, where necessary, the light curves were used to scale the optical, PUI, and MIPS data.

3.1.1. Comparison with Blackbodies at Days 64–464

At each IRAC epoch between 64 days and 464 days, blackbodies were matched to the underlying optical and MIR spectral

[14] These were obtained from the SUSPECT database: http://bruford.nhn.ou.edu/∼suspect/index1.html.

Table 3
Late-time Optical Magnitudes of SN 2004et

Date	MJD	Epoch†	Magnitudes				Source
		(d)	*B*	*V*	*R*	*I*	
2006 Dec 24	54093	823	22.65(20)	22.15(20)	21.65(20)	21.15(20)	Keck spectrum
2007 Apr 13	54203	933	. . .[a]	22.25(20)	21.55(20)	21.20(20)	Keck spectrum
2007 Jul 8	54289	1019	23.40(10)	23.20(10)	23.05(10)	22.85(10)	*HST*
2007 Aug 12	54324	1054	24.00(10)	23.49(8)	22.59(8)	22.55(12)	WHT
2007 Nov 12	54416	1146	22.85(20)	22.55(20)	22.00(20)	21.70(20)	Keck spectrum
Nearby stars			25.00(10)	24.30(10)	23.75(10)	23.00(10)	*HST*

Notes. Magnitudes derived from spectra obtained at the Keck telescope and from R. M. Crockett et al. (2009, in preparation) (*HST* and WHT). Uncertainties in the last two figures are shown in parentheses. The SN magnitudes have been corrected for the effects of two faint stars that lay within the seeing disk of the ground-based observations. The bottom line shows the combined magnitudes of the two stars derived from the *HST* magnitudes reported by R. M. Crockett et al. (2009, in preparation) (see text).

† Following Li et al. (2005), we assume an explosion date of 2004 September 22.0 (MJD = 53270.0).

[a] There is no *B* value on day 933 since at this epoch there was only partial coverage of the appropriate section of the spectrum.

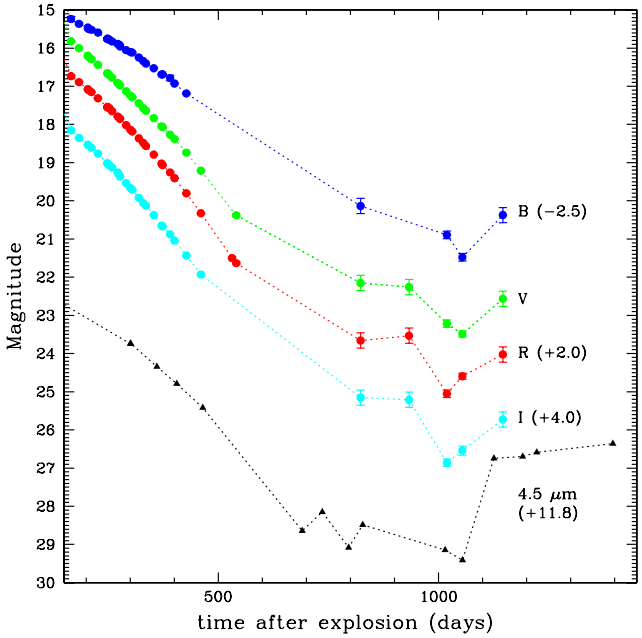

Figure 5. Late-time optical light curves of SN 2004et. The pre-600 day data are from Sahu et al. (2006), while the post-800 day magnitudes were estimated from spectra taken at the Keck telescopes (see Section 2.3), as well as from *HST* and WHT photometry (R. M. Crockett et al. 2009 (in preparation) (see text and Table 3). The light curves have been corrected for the effects of two faint stars that lay within the seeing disk. Also shown for comparison is the 4.5 μm light curve. For clarity, the *B*, *R*, *I*, and 4.5 μm plots have been shifted vertically by the indicated amounts.

(A color version of this figure is available in the online journal.)

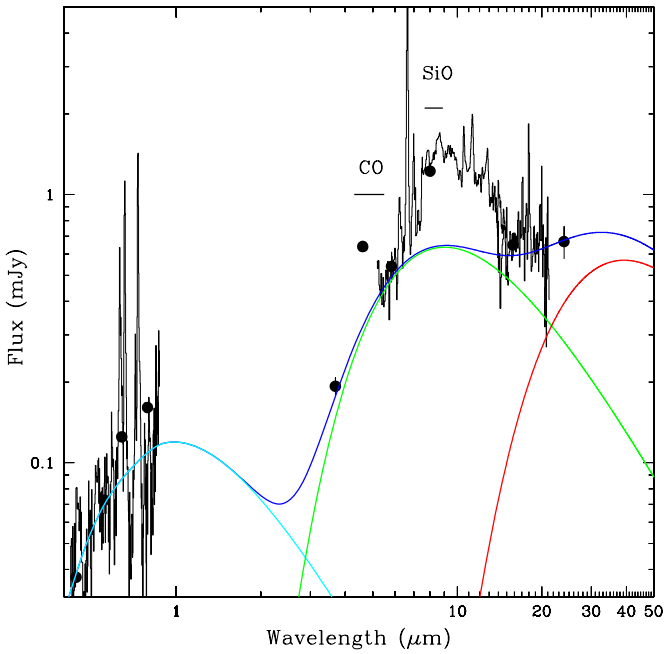

Figure 6. Three-component blackbody match to the day 464 spectral continua of SN 2004et. The combined blackbody spectrum is shown in blue while the hot, warm, and cold components alone are shown in cyan, green, and red (respectively). The blackbodies have been reddened according to the Cardelli et al. (1989) extinction law with $A_V = 1.0$ mag (see text). The optical spectrum is from Sahu et al. (2006), and the optical photometry is from Sahu et al. (2006) and Misra et al. (2007). The optical, PUI, and MIPS fluxes have been interpolated to day 464.

(A color version of this figure is available in the online journal.)

continua. For the day 64 epoch, it was found that a fair representation of the SED/spectral continua required just a single, hot blackbody. This is presumably due to the ejecta photosphere dominating the flux at this phase. There is little sign of thermal emission from dust. We first considered the match using $E(B-V) = 0.41 \pm 0.07$ mag (Misra et al. 2007, and references therein). For a Cardelli et al. (1989) law with $R_V = 3.1$, this corresponds to $A_V = 1.27 \pm 0.22$ mag. However, we found that assuming the same extinction law, it was impossible to obtain a match to the optical continuum without also significantly overproducing the MIR flux. We found that $A_V = 1.0$ mag provided a more satisfactory match and so this value was adopted throughout the paper, using the Cardelli et al. (1989) law with $R_V = 3.1$.

For the 300–464 day era, it was found that a reasonable representation of the spectral continua required three blackbodies: (1) a hot (5000–10000 K) blackbody to represent continuum optical emission from the hot ejecta, and (2) a combination of warm (450–700 K) and cold (100–130 K) blackbodies to represent the emission longward of ∼2.5 μm. As an example, in Figure 6 we illustrate the contributions of these three components for day 464. The blackbodies were matched to the observations as follows. The hot blackbody was first matched to the continuum of the optical spectrum. The principal purpose here was to estimate the effect that the hot continuum might have on the shorter wavelength MIR fluxes. In the *BV* region,

the continuum dominated and so the photometric points lay close to the continuum and the model. However, in the *RI* region, strong emission from lines of Hα, [O I] $\lambda\lambda$6300, 6464, and [Ca II] $\lambda\lambda$7291, 7323 meant that the photometric points lay above the continuum.

The warm and cold blackbodies were then matched to the MIR continuum. During days 300–464, no attempt was made to reproduce the fluxes around 4.5 μm or 8.0 μm, since these regions were strongly affected by CO and SiO emission. Moreover, the broad emission in the 8–14 μm range could not be matched by a simple blackbody. (We shall show below that this feature was due to silicate dust.) Consequently, the warm/cold blackbody match was primarily to the spectral continua around 6 μm and >14 μm plus photometry points at 3.6 μm (IRAC), 16 and 22 μm (IRS peakup imager), and 24 μm (MIPS). Iteration of the parameters of the three blackbodies was carried out to optimize the overall match.

3.1.2. Comparison with Blackbodies at Days 690–795

For IRAC days 690–795, the only reasonably contemporary optical spectrum was taken at the Keck telescope at day 823 (Figure 4). The optical spectrum comprises broad emission lines on top of quasi-continuum emission. At IRAC day 795, for the same reason as given above, the hot blackbody was adjusted to match the continuum only. Thus, while a good match to the *V* magnitude was obtained, it underproduced the total fluxes in the *B*, *R*, and *I* bands. Given the indirect evidence (see below) that the broad box-like profiles could have been influencing the spectrum as early as ~690 days, for epochs 690 and 736 days the hot blackbody parameters were guided by the match at 795 days (i.e., the model was adjusted to match the *V*-band flux but to underproduce in the *B*, *R*, and *I* bands). Only one MIR spectrum was available (day 823, scaled to IRAC day 795), spanning 5–15 μm. This showed little evidence of strong CO/SiO/silicate emission, although the spectrum is very noisy in the 5–7.5 μm region. We adjusted the warm/cold models to match the spectral continuum, or the photometry fluxes where there was no spectral coverage.

We note that the 8 μm flux on day 690 is underproduced by the model (Figure 7), suggesting that the silicate emission, while weaker, was still quite prominent at that epoch. At subsequent epochs, the excess at 8 μm continued to fade. Indeed, by day 736, the blackbody model provided quite a reasonable match in this wavelength region, consistent with the near disappearance of the silicate feature by then.

3.1.3. Comparison with Blackbodies at Days 1125, 1222, and 1395

For the final three epochs, a similar procedure was followed. At day 1125, the hot blackbody was matched to the 1146 day optical spectrum scaled to day 1125. For day 1222, the warm/cold blackbodies were matched to the day 1212 MIR spectrum scaled to day 1222. These matches were then used to guide the choice of blackbody parameters for, respectively, the Day 1125 MIR region and the day 1222 optical region. For the latest epoch the hot blackbody was matched to optical fluxes obtained by extrapolation of the *BVRI* light curves to day 1395, while the warm/cold blackbodies were matched to the IRAC, MIPS, and IRS data from the period around day 1395.

The complete set of blackbody matches for days 64–1395 is shown in Figure 7, and all of the blackbody parameters are listed in Table 4. Also shown is the evolution of the blackbody luminosities compared with the estimated total deposited radioactive

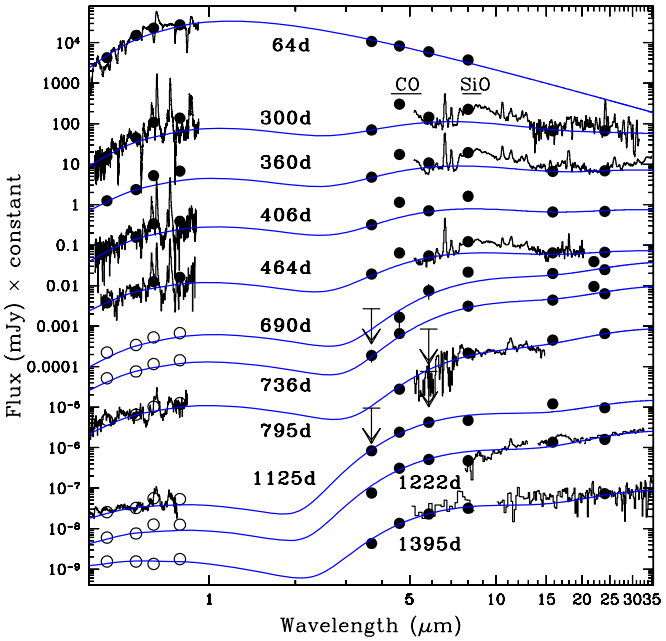

Figure 7. One-component (day 64) and three-component (days 300–1395) blackbodies (smooth continuous lines: see Table 4) compared with the optical and MIR spectra/SEDs of SN 2004et. The models have been reddened according to the Cardelli et al. (1989) extinction law with $A_V = 1.0$ mag. The photometry is indicated by filled circles. The PUI, MIPS, and spectral fluxes have been interpolated to the epochs of the IRAC observations. The open circles indicate estimated optical fluxes obtained by interpolation or extrapolation of the light curves. For day 690 and later, the optical data have been corrected for the effects of two faint stars that lay within the seeing disk (see text). The epochs are relative to the estimated explosion date of 2004 September 22.0 (Li et al. 2005, MJD = 53270.0). The plots have been shifted vertically for clarity.

(A color version of this figure is available in the online journal.)

luminosity due to ^{56}Ni, ^{57}Ni, and other radioactive species, assuming the deposition behavior specified by Li et al. (1993).[15] (Note: Since the blackbodies were matched to the continua only, their luminosities slightly underestimate the total luminosities.) Using the optical photometry around day 300 (Sahu et al. 2006) and the exponential tail method of Hamuy (2003), we estimate a ^{56}Ni mass of $0.055 \pm 0.020\ M_{\odot}$. This is about 10% less than the values found by Sahu et al. (2006) and Misra et al. (2007) and is due to our reduced value of A_V, partially compensated for by our slightly larger adopted distance.

On day 64 the hot component temperature was 5300 K and its luminosity exceeded that of the radioactive decay deposition by a factor of 3.8. These two points are consistent with emission from the recombination-determined photosphere during the plateau phase. Up to day 795, the hot component remained around 5000–7000 K, but its luminosity faded rapidly. A rise in apparent temperature and luminosity was seen on days 1222 and 1395. However, the optical fluxes at these epochs were obtained by uncertain extrapolation of the late-time light curves and so the blackbody parameters are approximate, especially at the later eoch.

The warm component cooled and faded monotonically between days 300 and 795. In addition, the blackbody surface never exceeded ~1600 km s^{-1}. Furthermore, the warm blackbody luminosity was less than or comparable with the radioactive input up to day 795. This behavior is consistent with the

[15] The ^{56}Co decay dominates the luminosity during most of the period studied, but by day 800 10% is due to ^{57}Co decay and the contribution from this isotope grows with time.

Table 4
Blackbody Parameters for Matches to SN 2004et SEDs

Epoch (d)	v_{hot} (km s^{-1})	T_{hot} (K)	v_{warm} (km s^{-1})	R_{warm} (10^{16}cm)	T_{warm} (K)	v_{cold} (km s^{-1})	T_{cold} (K)	L_{rad} (10^{38} erg s^{-1})	L_{hot} (10^{38} erg s^{-1})	L_{warm} (10^{38} erg s^{-1})	L_{cold} (10^{38} erg s^{-1})
64	3000	5300	...	...	...	...	...	4030	15470	...	...
300	66	6000	1600	0.41	700	12000	130	485	270	29	1.3
360	38	6500	1300	0.40	670	12000	130	255	180	23	1.4
406	28	6300	1250	0.44	610	11000	130	160	110	19	2.0
464	14	7000	1100	0.44	570	9500	130	86	54	15	2.6
690	3.3	6500	850	0.51	410	9000	110	7.6	4.9	5.2	2.4
736	2.6	7000	830	0.53	400	8500	110	4.8	4.7	5.1	2.7
795	2.2	7000	650	0.45	390	6500	120	2.6	3.9	3.3	2.9
1125	0.62	10000	510	0.50	500	6000	120	0.17	2.6	10.9	5.0
1222	0.83*	10000*	500	0.53	500	7000	120	0.10	5.5*	12.4	8.1
1395	1.07*	15000*	465	0.56	510	6000	120	0.05	60.0*	15.1	7.7

Notes. The blackbody luminosities (L_{hot}, L_{warm}, L_{cold}) are given in Columns 10–12. In Column 9, L_{rad} is the radioactive deposition luminosity corresponding to the ejection of 0.055 $M_{\odot}$ of ^{56}Ni, scaled from the SN 1987A case described by Li et al. (1993).
* The day 1222 and day 1395 optical parameters are approximate. They were obtained by blackbody matches to fluxes obtained through extrapolation of the optical light curves.

warm emission arising from newly formed dust in the ejecta and supports the optically based claims of Sahu et al. (2006) and Misra et al. (2007) that ejecta dust formation took place during this period. By day 1125, the warm component luminosity had *increased* by a factor of 3.3 since day 795 and exceeded the radioactive deposition by a factor of over 60. In addition, its temperature had risen slightly. These points imply that an additional energy source must have come into play. This will be discussed further in Section 3.2. An interesting point is that the warm blackbody radius remained constant to within ±17% throughout days 300–1395. This will also be examined later.

The cold component maintained a roughly constant temperature of 120 ± 10 K throughout the day 300–1385 era. The velocity declined monotonically from 12000 km s^{-1} on day 300 to ∼6000 km s^{-1} on days 1125–1395. The luminosity rose slowly during days 300–795, and then more rapidly during the final three epochs. The high velocities immediately rule out an origin for the cold component in newly formed ejecta dust. In particular, these velocities are derived from blackbody matches. Consequently, the velocities correspond to the smallest possible source radii consistent with the cool component SED. Yet the required velocities are still too large for the source to be attributable to ejecta dust. Also, again since these are blackbody matches, these results are independent of the nature of the dust. Furthermore, there is currently no known mechanism by which newly formed ejecta dust rapidly cools, leaving behind only a small warm component that is amenable to detection at MIR wavelengths. Nor is it clear that such a scenario could be made to be consistent with the optical depths indicated by the MIR spectra. We propose instead that, at least up to day 795, the cold component arose from dust whose existence preceded the supernova explosion. The obvious mechanism for this radiation is an IR echo.

3.2. More Detailed Interpretation of the IR Emission

Guided by the results of the blackbody study above, we carried out a more detailed investigation of the three components of the SN spectrum. Regarding the hot component, Wooden et al. (1993) showed that during the second year of SN 1987A, the dust-emission continuum could be contaminated by blackbody emission from hot, optically thick gas, as well as by free–bound radiation. Here we represent both effects using a single hot blackbody, as before. The hot blackbody was adjusted to match the underlying continuum of the optical spectrum as discussed above. The free parameters were blackbody radius (usually introduced as epoch and velocity) and temperature.

For the warm component, we note from the blackbody study that in the period 300–795 days, the IR emission is consistent with an origin in newly condensed ejecta dust, heated by radioactive decay. However, an alternative source could be dust in the progenitor wind (i.e., an IR echo), and we first examine this possibility. A comparison with IR echo models (Meikle et al. 2006) suggests that the warm component could indeed be due to reradiation of the SN flux from preexisting circumstellar dust. For a dust-free cavity formed by evaporation by the observed SN peak flux, over a range of CSM density profiles ($n = -1$ to -2.3), we find that the echo model light curve actually declines too rapidly. However, if we increase the cavity size by a factor of ∼10, then the IR echo model can reproduce the characteristic dust temperature and SED decline over the 300–795 days period. Such a large cavity would have to be the result of the episodic mass-loss history of the progenitor, or dust evaporation by the initial UV flash.

The problem with this scenario is the *ad hoc* nature of the "fine tuning" of the cavity size required to make it work. There is no independent evidence to support the occurrence of a mass-loss event or UV flash which yielded a cavity of just the right size to account for the warm-component behavior and support the IR echo scenario. On the contrary, Sahu et al. (2006) argue that line shifts to the blue in their late-time optical spectra imply dust formation in the ejecta. We have independently reexamined their spectra. In the [O I] λ6300 line, we find that during days 314–465 the red wing shifts by about 800 km s^{-1} to the blue while the blue wing is unmoved. We therefore agree with Sahu et al. (2006) that this is evidence of dust condensation in the ejecta.[16]

[16] In the Hα profiles, also presented by Sahu et al. (2006), between days 301 and 314 we find a jump of −400 km s^{-1} in the whole profile, but little sign of a progressive blueshift in the subsequent day 314–465 period. During this period, the shift remained at about −165 km s^{-1} (corrected for the redshift of NGC 6946). We suggest that this could simply be due to the peculiar velocity of the supernova center of mass. We have no explanation for the sudden day 301–314 jump. Nor do we see the "flattening" in the profile reported by Sahu et al. (2006). We conclude that there is little evidence of a progressive blueshift in the Hα line. However, given the highly extended nature of the hydrogen envelope, dust formed in the much smaller refractory-element zone of the SN would be unlikely to produce a significant modification of the profile, except perhaps a truncation of the extreme red wing.

In addition, Sahu et al. (2006) and Misra et al. (2007) found that in the period 310–370 days, the rate of decline in the optical light curves accelerated. Such behavior is also suggestive of dust condensation in the ejecta, although alternative explanations for the steepening are (1) increasing transparency of the expanding ejecta to the gamma rays from the radioactive decay, or (2) the onset of the IR catastrophe. Nevertheless, taken with the [O I] λ6300 blueshift and the necessarily specific selection of the cavity radius for the IR-echo model to work, we conclude that the warm component during days 300–795 was most likely due to newly formed, radioactively heated dust in the ejecta. We also note that no detectable IR echo would be expected from a dusty cool dense shell (CDS; see below), since the CDS would not have formed until long after the bulk of the SN UV/optical flux had passed.

3.2.1. The Warm Isothermal Ejecta Dust Model

We investigated the ejecta-dust hypothesis using a simple analytical IR-emission model (Meikle et al. 2007) comprising a uniform sphere of isothermal grains with the luminosity and SED obtained via the escape probability formalism (Osterbrock 1989; Lucy et al. 1989). At wavelengths beyond ∼14 μm we found that, as with the blackbody study, the warm isothermal dust model (IDM) increasingly underproduced the observed flux. Consequently, a cold component had to be included. Similar to the earlier blackbody study, we found that for the period 300–795 days the cold-component flux could be reproduced with a blackbody at ∼110 K, radius (3.0–5.5) × 10^{16} cm, and luminosity (2–3) × 10^{38} erg s^{-1}. The source of this radiation cannot be newly formed dust in the SN ejecta. To attain the required blackbody radius at a given epoch would require velocities as high as 12000 km s^{-1}, far greater than the velocities of the fastest-moving refractory elements. We therefore invoked an IR echo from preexisting dust to account for the cold component. This was based on the IR echo model of Meikle et al. (2006) and will be described in detail below.

To select the likely grain density distribution and grain materials for the IDM, we were guided by dust condensation calculations and the explosion models upon which they are based. Only a few papers have been published that describe local SN dust condensation based on explosion models. Kozasa et al. (1989) and Todini & Ferrara (2001) have calculated dust condensation within the ejecta of SN 1987A, while Bianchi & Schneider (2007) have examined dust formation in supernovae having progenitors of 12–40 $M_{\odot}$ and solar metallicity. These authors used the ejecta chemical composition as determined in nucleosynthesis models (Nomoto et al. 1991; Woosley & Weaver 1995). All adopted complete chemical mixing within the dust-forming zone. Within this zone, Todini & Ferrara (2001) and Bianchi & Schneider (2007) assumed a uniform density distribution, while Kozasa et al. (1989) used the density profile from an explosion model (Hashimoto et al. 1989), but this is also roughly flat. Dust-type abundances were determined by all the authors, but none made explicit predictions about the dust distribution within the ejecta. Three-dimensional core-collapse SN explosion models (Kifonidis et al. 2006) confirm that extensive mixing of the core takes place. In addition, the same models show that the density structure is likely to be exceedingly complex, with high-density clumps moving out through lower density gas. Qualitatively similar results are reported for jet-driven explosions of red supergiants by Couch et al. (2009). How this affects the dust distribution has yet to be determined.

Given the current state of knowledge, we assume that dust of uniform number density forms throughout the zone containing abundant refractory elements. The extent of this zone can be assessed using the late-time widths of metal lines. In the nebular optical spectra of SN 2004et (Sahu et al. 2006) the maximum velocities implied by the metal lines generally do not exceed ∼2500 km s^{-1}. This upper limit is adopted as the size of the dust-forming region. The uniform-density assumption is conservative in that it provides the least effective way of hiding dust grains in optically thick regions. We initially considered both silicate and amorphous carbon dust, with the mass absorption functions taken from Laor & Draine (1993) and Rouleau & Martin (1991), respectively.

The IDM comprises a uniform sphere of isothermal dust grains. Following the escape probability formalism (Osterbrock 1989; Lucy et al. 1989), the luminosity ($L(\nu)$) of the sphere at frequency ν is given by $L(\nu) = 4\pi^2 R^2 B(\nu, T)[0.5\tau(\nu)^{-2} \times (2\tau(\nu)^2 - 1 + (2\tau(\nu) + 1)e^{-2\tau(\nu)})]$, where R is the radius of the dust sphere at some time after the explosion, $B(\nu, T)$ is the Planck function at temperature T, and $\tau(\nu)$ is the optical depth to the center at frequency ν. For a grain-size distribution $dn = ka^{-m}da$, where dn is the number density of grains having radius $a \rightarrow a + da$, m is typically between 2 and 4, and k is the grain number density scaling factor, it can be shown that $\tau(\nu) = \frac{4}{3}\pi k\rho\kappa(\nu)R\frac{1}{4-m}[a_{(\mathrm{max})}^{4-m} - a_{(\mathrm{min})}^{4-m}]$, where ρ and $\kappa(\nu)$ are, respectively, the density and the mass absorption coefficient of the grain material. The grain-size distribution law was set at $m = 3.5$ (Mathis et al. 1977) with $a_{(\mathrm{min})} = 0.005$ μm and $a_{(\mathrm{max})} = 0.05$ μm. The total mass of dust, M, was then found from $M = 4\pi R^2\tau(\nu)/3\kappa(\nu)$ (Lucy et al. 1989). For a given grain material (silicate or amorphous carbon), the free parameters were grain temperature and grain number density scaling factor, k.

3.2.2. Comparison of the IDM with the Observations

We found that to achieve reasonable matches to the data, it was necessary to increase the dust mass until it was optically thick in the MIR. To make use of the much greater information available in the MIR spectra (compared with the photometry), we first carried out model matches to those epochs for which we had both MIR spectra and reasonably contemporary photometry (see above). This comprises six epochs, corresponding to IRAC days 300, 360, 464, 795, 1222, and 1395. The parameters of the hot blackbody, warm IDM, and cold IR echo components were adjusted to optimize the overall match to the continua. Guided by these results, model matches were carried out for the remaining epochs where no MIR spectra were available. We examined the warm-model matches using silicate and amorphous carbon grain materials.

(a) 300–464 days. An inspection of the day 300, 360, and 464 MIR spectra suggests the presence of SiO fundamental emission in the 7.7–9.5 μm region. SiO was discovered in the Type II-pec SN 1987A (Roche et al. 1991; Wooden et al. 1993) and more recently in the Type II-P SN 2005af (Kotak et al. 2006). To assess the contribution of SiO in SN 2004et we added an SiO component to the silicate model spectrum. The SiO models were taken from a study of SiO in SN 1987A by Liu & Dalgarno (1994). We used their non-LTE (local thermodynamic equilibrium) models whose epochs lay most closely in time to the above three SN 2004et observation epochs in the day 300–464 period, and SiO masses were estimated assuming similar excitation conditions in the two SNe. The coexistence of SiO and silicates is not surprising since SiO formation is an essential

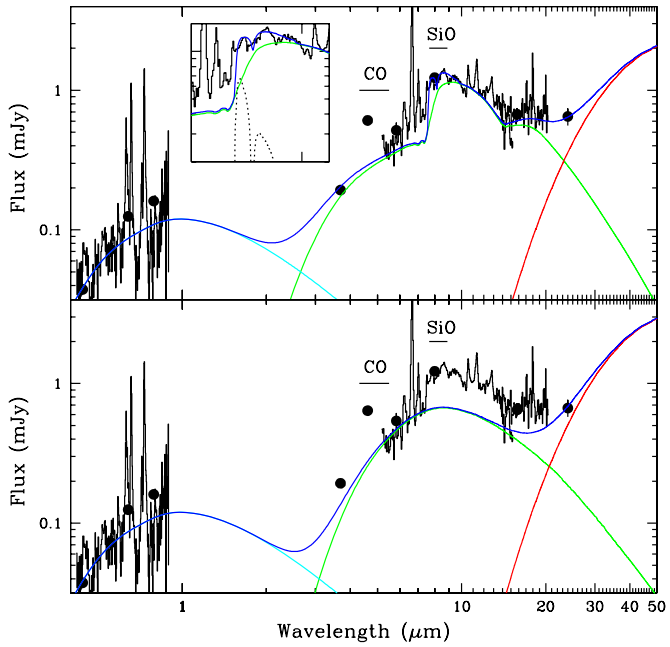

Figure 8. Day 464 observations (black) of SN 2004et compared with models. The upper (main) and lower panels show the IDMs (green) for silicate and amorphous carbon grains, respectively. The total model spectrum (blue) also comprises hot (blackbody: cyan) and cold (interstellar IR echo: red) components. The upper panel model also contains a contribution from the SiO fundamental. The inset shows the separate SiO contribution (dotted line). It can be seen that a superior match to the spectrum is achieved with the combined silicate dust and SiO model, as compared with the amorphous carbon dust model.

(A color version of this figure is available in the online journal.)

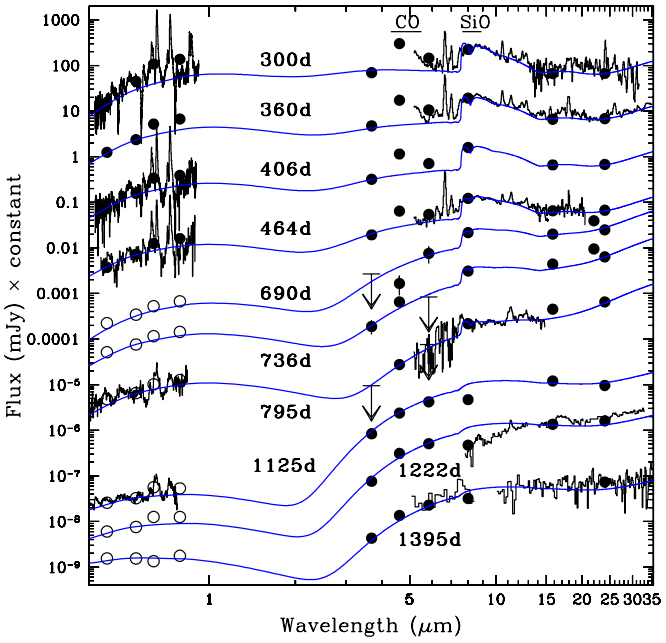

Figure 9. Silicate dust models (smooth continuous lines) compared with MIR SEDs of SN 2004et (see Table 5). The models also comprise hot (blackbody) and cold (interstellar IR echo) components (see text). The models have been reddened according to the Cardelli et al. (1989) extinction law with A_V = 1.0 mag. The photometry is indicated by filled circles. The PUI, MIPS, and spectral fluxes have been interpolated to the epochs of the IRAC observations. The open circles indicate estimated optical fluxes obtained by the interpolation or extrapolation of the light curves. For day 690 and later, the optical data have been corrected for the effects of two faint stars that lay within the seeing disk (see text). The epochs are relative to the estimated explosion date of 2004 September 22.0 (MJD = 53270.0) (Li et al. 2005). The plots have been shifted vertically for clarity.

(A color version of this figure is available in the online journal.)

step in the silicate-formation sequence (e.g. Todini & Ferrara 2001). No SiO was added to the amorphous carbon version of our model.

In order to reproduce the fading visibility of the silicate feature during the 300–464 day period, it was necessary to increase the optical depth. We found that $\sim 0.5 \times 10^{-4}\ M_\odot$ of silicate grains plus a few $\times 10^{-4}\ M_\odot$ of SiO provided good matches to the MIR continua. The carbon models also required $\sim 10^{-4}\ M_\odot$ of dust, but they produced much inferior matches to the continua, especially in the 8–14 μm region. Examples of matches at day 464 for the two grain materials are shown in Figure 8. All of the three-component model matches for silicate grains are shown in Figure 9, and the silicate model parameters are summarized in Table 5.

The success of the silicate model in reproducing the 8–14 μm feature during days 300–464 provides strong support for the newly formed silicate dust scenario, at least for this period. The dust temperature fell from 900^{+100}_{-140} K to 650^{+50}_{-50} K. Even as early as day 300, the optical depth to the center at 10 μm ($\tau_{10\mu\mathrm{m}}$) had to be set as high as 2.8 in order to reduce the silicate feature to the observed visibility. By day 464, the optical depth had increased to 3.6. Also, the dust mass had grown to $(0.66^{+0.27}_{-0.15}) \times 10^{-4}\ M_\odot$.

An interesting point about the mass estimates is that the silicate feature yields an additional constraint on the model at each epoch since the optical depth had to be adjusted to match the visibility of the observed 8–14 μm feature. Consequently, in spite of the high optical depth, within the uniformity limitation of the model the derived dust masses are actual values rather than just lower limits. Moreover, since the optical depth, $\tau(\nu)$, is fixed by the silicate feature visibility and the dust mass $M \propto \tau(\nu)$ (see above), it follows that the dust mass is insensitive to the grain-size limits. We also stress that in the silicate dust model, most of the observed broad 7.5–14 μm emission feature is produced by silicate. SiO makes a relatively minor contribution (see Figure 8). Nevertheless, the SiO mass was more than adequate to supply the material for the newly formed silicate dust. This supports the newly formed silicate grain hypothesis. The SiO decline from about $6 \times 10^{-4}\ M_\odot$ to $3.5 \times 10^{-4}\ M_\odot$ over the period may also suggest that it was indeed supplying the silicate material. However, it is possible that some of the mass decline was not real but was actually due to reduced excitation as the ejecta cooled from 900 K to 650 K during this period.

(b) 690–795 days. While we conclude that, up to at least day 464, the newly formed grains in the ejecta of SN 2004et were dominated by silicate material, the situation at later epochs is somewhat less clear. From day 690 onward, the visibility of the 8–14 μm silicate feature faded quite rapidly. Indeed, by day 795 there may only be a small excess remaining in the silicate region. The fading of the silicate feature could be due to (1) increasing optical depth as more silicate dust forms, or (2) an increasing contribution of IR emission from non-silicate dust in a cool dense shell (CDS) formed by an ejecta/CSM collision. A third possibility is the suppression of the silicate feature by the increased prominence of emission from undisturbed non-silicate CSM dust. However, we have already dismissed above the likelihood of a *warm* IR echo, so this mechanism is not considered further. From as early as day 690, the hot+warm component increasingly exceeded the radioactive input luminosity. Indeed, since the models were matched to the continua only, the true hot+warm luminosities are even a little larger than those shown in Table 5. The growing luminosity

Table 5
Model (Silicate) Parameters for Matches to SN 2004et Observations

Epoch (d)	$v_{\rm hot}$ (km s^{-1})	$T_{\rm hot}$ (K)	$v_{\rm warm}$ (km s^{-1})	$R_{\rm warm}$ (10^{16} cm)	$T_{\rm warm}$ (K)	$\tau_{10\mu m}$	$L_{\rm rad}^{\dagger}$ (10^{38} erg s^{-1})	$L_{\rm hw}^{\dagger\dagger}$ (10^{38} erg s^{-1})	$L_{\rm warm}$ (10^{38} erg s^{-1})	$M_{\rm dust}$ ($10^{-4}\,M_{\odot}$)	$M_{\rm SiO}$ ($10^{-4}\,M_{\odot}$)
300	61	6000	1700	0.44	900	2.8	485	271	40.5	0.39	5.7
360	38	6500	1600	0.50	730	3.1	255	202	25.4	0.57	5.8
406	25	6700	1420	0.50	700	3.3	160	132	22.0	0.60	4.1
464	14	7000	1250	0.50	650	3.6	86	71.6	17.7	0.66	3.7
690	3.3	6500	800	0.48	500	5.2	7.6	12.5	7.1	0.85	∼0.9
736	2.6	7000	680	0.43	450	6.6	4.8	9.5	4.3	0.90	∼0.6
795	2.2	7000	620	0.43	400	11.5	2.6	6.5	3.3	1.5	∼0.5

Notes. As discussed in the text, by day 1125 our model is no longer appropriate; hence, we do not list the parameters for days 1125, 1222, or 1395 above. Typical silicate model uncertainties: day 300: $v_{\rm warm} = 1700^{+300}_{-200}$ km s^{-1}, $T_{\rm warm} = 900^{+100}_{-140}$ K, $M_{\rm dust} = (0.39^{+0.25}_{-0.12}) \times 10^{-4}\,M_{\odot}$; day 464: $v_{\rm warm} = 1250^{+150}_{-100}$ km s^{-1}, $T_{\rm warm} = 650^{+50}_{-50}$ K, $M_{\rm dust} = (0.66^{+0.27}_{-0.15}) \times 10^{-4}\,M_{\odot}$; day 795: $v_{\rm warm} = 620^{+130}_{-70}$ km s^{-1}, $T_{\rm warm} = 400^{+20}_{-40}$ K, $M_{\rm dust} = (1.5^{+1.2}_{-0.4}) \times 10^{-4}\,M_{\odot}$.

† $L_{\rm rad}$ is the radioactive deposition luminosity.

†† $L_{\rm hw} = L_{\rm hot} + L_{\rm warm}$.

excess relative to the radioactive input implies that an additional energy source must have come into play by day 690. A possible explanation for the MIR brightening is IR emission from dust produced in a shock-formed CDS due to ejecta/CSM collision (see below). Such a phenomenon was invoked to account for IR emission from SN 1998S (Pozzo et al. 2004) and SN 2006jc (Smith et al. 2008; Mattila et al. 2008).

An ejecta/CSM collision would also account for the appearance of the wide, box-like ("square") emission-line profiles in the optical region as well as the rebrightening of the optical light curves. As mentioned above, given the large decline in the supernova optical flux between days 465 and 823, it is difficult to determine when the wide components actually appeared. However, given that we see the light curve leveling off by ∼800 days, it seems likely that the box-like profiles emerged at about the same time. Similar box-like profiles were seen in the H and He lines of the Type IIn SN 1998S albeit with a much earlier onset (Gerardy et al. 2000; Leonard et al. 2000; Pozzo et al. 2004), as well as in the Type IIb SN 1993J (Matheson et al. 2000; Fransson et al. 2005). For SN 1998S, Gerardy et al. (2000) proposed that the box-like profiles were due to an ejecta/CSM collision. We suggest that here, too, the appearance of the box-like profiles in SN 2004et was produced by the impact of the fastest-moving ejecta on a preexisting CSM. From the epoch and velocity of the wide Hα component, we can infer a shell of radius 8×10^{16} cm or 5600 AU at day 1146. For a red supergiant wind of velocity 10 km s^{-1}, this would indicate a CSM age of ∼2700 yr.

The appearance of the boxy profiles of Hα, [Ca II], and [O I] by day 800 puts constraints on the density of the circumstellar environment of SN 2004et. A requirement for a CDS to form behind the reverse shock of the supernova is that the cooling time of the shock is shorter than the adiabatic time scale. The cooling time can be estimated as $t_c = 4.6 \times 10^{-3} \dot{M}_{-5}/u_{\rm w1}^{-1} V_{\rm s4}^{5.34} t_{\rm days}^2$ days (Chevalier & Fransson 2003), which is valid for a power-law ejecta with $\rho \propto V^{-11.7}$, typical of a red supergiant progenitor. The requirement that the reverse shock should be radiative until at least day 1150, as indicated by the last spectrum, and using $V_s \approx 10^4$ km s^{-1}, translates into a requirement that $\dot{M} \gtrsim 2 \times 10^{-6}\,M_{\odot}$ yr^{-1} for $u_w = 10$ km s^{-1}. This is in agreement with both the value of $\dot{M} \approx 1 \times 10^{-5} (T_{\rm CSM}/10^5 {\rm K})^{0.75}\,M_{\odot}$ yr^{-1} from the radio observations (Chevalier et al. 2006) and from the X-ray observations, $(2 - 2.5) \times 10^{-6}\,M_{\odot}$ yr^{-1} (Rho et al. 2007). The former depends on the temperature of the circumstellar medium, $T_{\rm CSM}$, which is likely to be in the range $(2–10) \times 10^4$ K, resulting in at least the same mass-loss rate as the X-ray observations. We therefore conclude that the appearance of the boxy line profiles from the CDS is fully consistent with previous mass-loss determinations from this object. It is, however, interesting that SN 2004et is the first SN II-P for which this has been observed.

The question now arises: when did the CDS dust begin to significantly affect the MIR emission? Between days 300 and 795 the IDM luminosity (Table 5) declined roughly exponentially with a ∼200 day e-folding time. There is little sign of an increase in this time constant even as late as day 795, such as one might expect if CDS dust emission was becoming important. We also note that even as late as day 736 the IDM luminosity was less than that of the radioactive deposition, although by day 795 it exceeded it by ∼25%. We therefore suggest that, while the ejecta/CSM impact probably began as early as day 690, significant emission from CDS dust began somewhat later, at about day 800.

Thus, we decided that the IDM could provide useful estimates of the ejecta dust mass up to day 795. We matched the warm component allowing the silicate feature visibility to take as large a value as was consistent with the data. Up to day 795 we were still able to obtain fair matches to the data. The apparent decline in the mass of SiO continued, suggesting the ongoing removal of the molecules to form silicate grains. However, as in the day 300–464 period, some of the decline in the SiO feature may have been due to ejecta cooling. Compared with earlier epochs, the temperature declined more slowly, reaching 400^{+20}_{-40} K, and the 10 μm optical depth increased more rapidly, reaching 11.5. The dust mass also increased more rapidly, reaching $(1.5^{+1.2}_{-0.4}) \times 10^{-4}\,M_{\odot}$ at day 795. Given the weakness of the silicate feature by this epoch, our value should really be treated as an upper limit. However, it should also be kept in mind that, by this time, some of the MIR flux may have been due to the CDS dust, reducing the amount of directly observed ejecta dust that is inferred.

(c) 1125, 1222, and 1395 days. Between days 795 and 1125, the IDM luminosity increased by a factor of 5, exceeding the radioactive deposition by a factor of ∼100. Nevertheless, for completeness, we continued the IDM matching in the day 1125–1395 era. On days 1125 and 1222, the model used above provided a much less satisfactory fit to the SED (Figure 9). In particular, the model now overproduced in the 8 μm region.

Indeed, there is some evidence that the previously observed silicate emission feature evolved into an absorption component. The model could not reproduce this effect. However, by day 1395 the "absorption" had largely disappeared and a better model match was obtained. Nevertheless, we conclude that by day 1125 the uniform-density ejecta dust-emission model was no longer appropriate. In any case, as already indicated, by this epoch the vast bulk of the warm-component flux could not have been due to new, radioactively heated ejecta dust, and was probably due instead to CDS dust.

The optical spectra also provide evidence for the presence of CDS dust. The tops of the box-like profiles in the day 823–1146 optical spectra (Figure 4) exhibit a decline from the blue to the red, suggesting the presence of dust attenuation within the emission region. The large, high velocity widths of the boxy features in SN 2004et immediately rule out new ejecta dust as being the main source of the attenuation. Fading across the H and He profiles was also seen in SN 1998S. Pozzo et al. (2004) showed that the attenuation was probably due to dust that condensed in a CDS formed behind the reverse shock. We conclude, therefore, that the later MIR rebrightening was due to IR emission from dust formed in the CDS. As the ejecta shock moved into the CSM, a CDS was formed where dust could condense, resulting in the blue-to-red fading in the line profile and producing the excess infrared flux.

To make a rough estimate of the CDS dust mass present during the day 1125–1395 period, we applied the IDM to a shell of dust lying at 6000 AU. Adjusting the model to reproduce the MIR SEDs suggests CDS dust masses of $\sim 5 \times 10^{-4}\,M_{\odot}$ (amorphous carbon) or $\sim 2 \times 10^{-4}\,M_{\odot}$ (silicates). Such masses of the required refractory elements could be produced by a progenitor wind. The corresponding temperatures and optical depths at 10 μm are 330 K and $\sim$0.03 for amorphous carbon and 500 K and $\sim$0.025 for silicates. The corresponding V-band optical depths are 0.6 (amorphous carbon) and 0.015 (silicates). These are in addition to the $A_V = 1.0$ mag, which was present before the CDS formation. We note that while the CDS model can provide a fair representation of the fluxes over most of the MIR range covered, in the 8–14 μm region the observed "dip" is not reproduced. Indeed, the silicate match is very poor in this region owing to the strong silicate emission feature. The observed dip may be a sign that the dust in the CDS has actually condensed into optically thick clumps which, if silicate in composition, might produce a broad absorption in this region. The CDS dust masses for SN 2004et are about a factor of 10 less than the lower limit for the CDS dust mass obtained by Pozzo et al. (2004) for the Type IIn SN 1998S. However, at about 8×10^{16} cm, the radius of the SN 2004et CDS is much larger than the $\sim 1.5 \times 10^{16}$ cm CDS radius in the case of SN 1998S. Further investigation of the CDS is beyond the scope of this paper.

3.2.3. Dust Clumping

An intriguing result from both the warm blackbody models and IDMs is the remarkable constancy (standard deviation <10%) of the model radii throughout the day 300–795 era (Tables 4 and 5), during which time the SN itself expanded by a factor of 795/300 = 2.65. How might this occur? Given the assumed uniform density, the high optical depth throughout the period implies that the MIR "photosphere" would always lie quite close to the physical surface of the radiating dust extent of the model. It is therefore conceivable that, if the photospheric radius remained fixed, as the ejecta flowed through it the model radius would also remain roughly constant. But for this scenario to work, the dust flowing beyond the photosphere would have to be replaced within the photosphere at just the right rate to maintain the fixed photospheric radius. This seems to be a rather contrived scenario. A more plausible explanation is that the dust actually formed in small, dense, comoving clumps. Such clumps might arise in localized regions of density enhancement. With more efficient cooling in such regions, the clumps might be unable to expand against the hotter, higher pressure interclump gas. We know that in the case of SN 1987A, there is strong evidence that the dust formed in clumps (Lucy et al. 1991).

Table 6
Parameters for Cloud of Silicate Dust Clumps Model Matches

Epoch (d)	$T_{\rm warm}$ (K)	$R_{\rm cl(max)}$ (10^{14}cm)	f ($\times$100)	$\tau_{\rm cl(max)}$ at 10 μm	$\tau_{\rm cd}$ at 10 μm	$M_{\rm dust}$ ($10^{-4}\,M_{\odot}$)	$M_{\rm SiO}$ ($10^{-4}\,M_{\odot}$)
300	900	1.83	1.4	2.6	0.43	0.40	5.7
360	730	1.95	1.0	3.5	0.36	0.61	5.8
406	700	2.10	1.84	3.0	0.32	0.61	4.1
464	650	1.91	0.43	4.1	0.21	0.69	3.7
690	500	1.63	0.084	8.2	0.07	0.99	$\sim$0.9
736	450	1.43	0.046	11.6	0.05	1.1	$\sim$0.6
795	400	1.53	0.044	13.0	0.05	1.4	$\sim$0.5

Note. With $m_1 = 0$, $R_{\rm cl(min)} = 0.01 R_{\rm cl(max)}$, $v_{\rm warm} = 2500$ km s^{-1}, and $N_{\rm cl} = 2500$.

In order to explore the effects of clumping on the MIR SED, we extended the silicate IDM so that it comprised clumps of dust grains and calculated the SEDs for days 300–795. We considered a spherical "cloud" of spherical clumps, with a cloud radius of $R_{\rm cd}$. The clumps are uniformly distributed within the cloud. At any given time, each clump has the same uniform number density of dust grains. The free parameters of the grains are the same as for the IDM: m, k, $a_{\rm (max)}$, and $a_{\rm (min)}$. For this study, the grain number density is allowed to vary, but m, $a_{\rm (max)}$, and $a_{\rm (min)}$ are fixed at the same values as adopted for the IDM described earlier. The SED was then derived using a treatment analogous to that of the uniform IDM. A clump-size distribution, $dn_{\rm cl} = k_1 R_{\rm cl}^{-m_1} d R_{\rm cl}$ is invoked, where $dn_{\rm cl}$ is the number density of clumps having radius $R_{\rm cl} \rightarrow R_{\rm cl} + d R_{\rm cl}$, and k_1 is the clump number density scaling factor (i.e., it controls the total number of clumps in the cloud, $N_{\rm cl}$). Thus, the free parameters of the clumps are m_1, $R_{\rm cl(max)}$, $R_{\rm cl(min)}$, and $N_{\rm cl}$. The model is restricted to the case of nonmerging clumps. The cloud radius is fixed at $v \times t$, where $v = 2500$ km s^{-1}, this being the extent of refractory elements indicated by the metal lines (see above). The SiO contributions were assumed to be the same as in the IDM case. For the hot and cold components, we used the same hot blackbody and echo model results as before. Details of the cloud of clumps model are given in the Appendix.

The cloud of clumps model was matched to the data using the same criteria as for the IDM case. We considered a simple case where $m_1 = 0$ (a flat number density distribution of clumps). For a given $N_{\rm cl}$, the model match to the SED is obtained by adjusting $R_{\rm cl(max)}$ and the grain number density. This match can be maintained over a wide range of $N_{\rm cl}$ by adjusting the clump radius and dust density so that the total dust mass is unchanged. In this study we fixed $N_{\rm cl} = 2500$ for all epochs. The total dust mass was also insensitive to the choice of $R_{\rm cl(min)}/R_{\rm cl(max)}$, and this was set at 0.01. Using the same model temperatures as for the IDM, virtually identical matches to those of the IDM were obtained. The cloud of clumps parameters are listed in Table 6.

As expected, there was little change in clump radii with time. $R_{\rm cl(max)}$ first rose to 15% above and then fell to ∼20% below the value at 300 days. The filling factor, f, defined as the ratio of the volume of clumps to that of the cloud, fell monotonically from 1.4×10^{-2} to 0.044×10^{-2}. The clump optical depth evolution at 10 μm increased almost monotonically with time, with the largest clumps closely matching the high optical depths of the IDM. In contrast, the optical depth of the cloud decreased from 0.4 to 0.05. As with the single-sphere IDM, the need to reproduce the silicate feature placed strong constraints on the model. For example, if we decreased the clump optical depths, and at the same time increased the cloud optical depth to maintain the overall level of the SED, the silicate feature was increasingly suppressed below the observed visibility. The reverse procedure produced a silicate feature that was too strong. The total dust mass was very similar to that of the IDM, increasing monotonically from $0.4 \times 10^{-4}\ M_\odot$ to $1.4 \times 10^{-4}\ M_\odot$. These results are as would be expected for a scenario where dust continues to form in clumps of fixed size and where the clumps are comoving with the expansion of the supernova.

It has been believed for some time that clumping occurs in SN ejecta (e.g., Lucy et al. 1991; Hachisu et al. 1991; Herant & Woosley 1994). Moreover, Fesen et al. (2001) have directly observed small knots [$(1–2) \times 10^{-4}$ of the extent of the dust-rich ejecta] in the SNR Cassiopeia A. However, the size distribution and evolution of such clumps is not well understood and does not allow us to constrain the clump model for SN 2004et. Nevertheless, at least for a flat number distribution of uniform-density clumps, we find that the introduction of clumping has a negligible effect on the estimated mass of dust. In particular, for the 300–465 days period, the derived masses are actual values rather than upper limits. It may be that by introducing nonuniform densities within the clumps, larger dust masses could be consistent with the observations, but such calculations are beyond the scope of this paper. Nevertheless, this brief study of the effects of clumping adds to the growing weight of evidence that the mass of grains produced in supernova ejecta can be only a minor contributor to the total mass of cosmic dust.

3.2.4. Interpretation of the Cold Infrared Source

To investigate the possibility that the cold component was due to an IR echo from pre-explosion dust, we used an IR-echo model similar to that described by Meikle et al. (2006). The model follows those of Bode & Evans (1980), Wright (1980), Dwek (1983), and Graham & Meikle (1986). The input bolometric light curve is a parametrized version of the *UBVRI* "bolometric" light curve (BLC) of Sahu et al. (2006): $L_{\rm bol} = L_0 \exp(-t/\tau)$, where $L_0 = 6.31$, $\tau = 26.3$ days for $0 < t < 46.0$ days, $L_0 = 1.80$, $\tau = 103.7$ days for $46 < t < 103.5$ days, $L_0 = 13400$, $\tau = 140.0$ days for $103.5 < t < 140.0$ days, $L_0 = 3.51$, $\tau = 108.9$ days for $140.0 < t < 429.5$ days, and $L_0 = 0$ for $t > 429.5$ days. L_0 is in units of 10^{42} erg s^{-1}. We caution that, owing to the omission of the SN flux outside the *UBVRI* range, this input probably underestimates the true total luminosity. Shortward of the U band, the input function may be only ∼0.5 of the true peak luminosity, but was probably closer to reality during the plateau phase. At wavelengths longer than the I band, the input function may underestimate the true luminosity by just ∼5% in the peak but up to 30% during the plateau. However, at these wavelengths the absorptivity of the dust grains (size ∼0.1 μm) is likely to have fallen well below unity. In the IR-echo results presented here we conservatively use just the *UBVRI* BLC.

Preliminary runs of the IR-echo model showed that, for typical grain radii (0.05–0.5 μm), to reproduce the cold component of the SN SED the dust had to lie at least 10 pc from SN 2004et. In a simple, spherically symmetric IR-echo model, a dust mass of ∼350 $M_\odot$ was required to yield the necessary luminosity, corresponding to a total mass of ∼60000 $M_\odot$. Clearly such a large mass could not have arisen in the progenitor CSM. Indeed, such a mass would be exceptionally large even for a star-formation nebula. A more natural explanation is that the cold component is due to an IR echo from interstellar, rather than circumstellar or otherwise local, dust. Supernova-triggered interstellar IR echoes were first predicted by Bode & Evans (1980) and Wright (1980).

In our interstellar IR-echo model, we invoked a uniform dust density extending from 10 pc (see above) to 100 pc from the supernova. Evaporation by the observed peak SN luminosity would be unlikely to produce a cavity exceeding ∼0.1 pc. However, a 10 pc cavity could have been caused by the progenitor wind or by neighboring stars. The 100 pc outer limit was chosen as the typical scale height of interstellar dust in a late-type spiral. (The host galaxy, NGC 6946, is practically face-on.) For ease of computation, the spherically symmetric geometry of the IR-echo model was retained. While not appropriate in general for the outer, presumably planar, limits of the dust in the galactic disk, for the early era being considered (∼3 yr relative to the SN-cavity-edge-SN light travel time of 65 yr) spherical symmetry provides a good approximation; at this epoch, the echo ellipsoid is extremely elongated (small minor/major axis ratio), and so the region of the spherical model outer surface intercepted by the ellipsoid is small and well approximates a plane surface. The outer radius is relatively uncritical for the match to the data: reducing the outer radius by 35% reduces the 24 μm flux by just 20%. For ease of computation, we assumed that the grain material was amorphous carbon where, for wavelengths longer than $2\pi a$, the grain absorptivity/emissivity can be well approximated as being proportional to $\lambda^{-1.15}$ (Rouleau & Martin 1991). For shorter wavelengths, an absorptivity/emissivity of unity was used. Also, for simplicity a single grain size was assumed. A material density of 1.85 g cm^{-3} was adopted (Rouleau & Martin 1991).

In matching the IR-echo model to the cold residual in the data, the free parameters were (1) the grain size, which influenced the typical dust temperatures; and (2) the grain number density, which determined the luminosity. For gas densities of 0.7 ± 0.3 cm^{-3} and maintaining a 0.006 dust/gas mass ratio, fair fits to the residual were achieved with grain radii in the range 0.2–0.005 μm with corresponding cavity radii of 8–16 pc and optical depths to UV/optical photons of 0.06–0.1. For grain radii less than ∼0.02 μm, the absorption cross section to UV/optical photons falls below the geometrical value, so for grains smaller than 0.02 μm the cavity radius had to be fixed at about 16 pc in order to prevent the dust temperature becoming too low. In addition, for grain radii less than 0.02 μm, the total optical depth to the UV/optical photons converged on a value of about 0.1. For cavity radii less than 8 pc, to prevent the dust temperature becoming too high, the grain size had be increased beyond 0.2 μm with a consequent increasingly implausible rise in interstellar medium (ISM) gas density above 1 cm^{-3}. We adopted a grain radius of 0.1 μm, yielding a grain number density of $(0.7 \pm 0.1) \times 10^{-12}$ cm^{-3} and an ISM gas density of 0.6 ± 0.1 cm^{-3}. This is a typical density for the gas disk of a late-type galaxy such as NGC 6946. The optical depth to UV/optical photons is about 0.07, which is easily encompassed

within the total $A_V = 1.0$ mag derived above. The temperature of the dust grains at the inner cavity edge is 125 K.

In Figure 8, upper panel, we show the model (silicate IDM) match for 464 days and note that by 24 μm the IR echo contributes more than half the total flux. In Figure 9, where all of the total three-component model matches (silicate IDM) are shown, it is particularly striking that the long-wave region ($\lambda \geqslant 20$ μm) is well reproduced by an IR-echo model having a *single* set of parameters for all epochs in the 300–795 day period. Even at days 1125, 1222, and 1395, the long-wave flux is reasonably reproduced by the IR echo. We conclude that the cold component is indeed caused by an IR echo from interstellar dust.

Finally, we note that Wooden et al. (1993) included free–free and free–bound emission in their model of the IR continuum of SN 1987A. They found that up to about 415 days post-explosion the free–free radiation dominated the total flux longward of ~30 μm. Their model did not include possible emission from an interstellar IR echo. We examined the possible contribution of free–free plus free–bound emission to the SN 2004et spectrum. We assumed that such emission was dominated by ionized hydrogen in the SN 2004et ejecta. The total (ionized+neutral) mass of hydrogen was assumed to be in the range of 1–10 $M_\odot$ and its extent was inferred from the Hα line widths. The number density and temperature were adjusted to find the maximum free–free plus free–bound flux, which was consistent with the optical to MIR observations and with the adopted hydrogen mass range. Within these constraints, an electron temperature of 4400–4700 K was obtained at 301 days cooling to 3850–4100 K at 795 days. We found that, prior to the ejecta/CSM collision, free–free emission could account for up to ~20% of the total 24 μm flux at 301 days, declining to less than 1% by 796 days. We conclude that the long wavelength continuum of SN 2004et was dominated by interstellar IR echo emission.

We would expect the IR-echo luminosity to remain approximately constant until the vertex of the echo ellipsoid reaches the boundary of the dust-free cavity. This would be in a time given by $R_{\rm in} = ct/2$, where $R_{\rm in}$ is the cavity radius. For the 10 pc dust-free cavity adopted above, and assuming a uniform dust density 10–100 pc from the supernova, we can expect the echo luminosity to remain constant for about 65 yr. We would also expect the apparent diameter of the echo to grow with time. At the latest epoch (day 1395) the echo would appear as an annulus having inner and outer diameters of about 0.″3 and 1.″0, respectively. This is well below the spatial resolution of *Spitzer* at 24 μm. However, for the next ~10 yr the annulus would grow roughly as $\sqrt{t}$. Thus, an additional test of the IR-echo hypothesis would be, in future missions, to attempt to detect and spatially resolve the MIR emission from SN 2004et.

4. CONCLUSION

We have presented the first-ever comprehensive MIR study of a Type II-P supernova, the most common of all SN types. Relative to the fluxes at optical wavelengths, the MIR luminosity of SN 2004et exhibited a strong and growing excess between 300 and 1395 days past explosion. We have shown that this is due to three types of supernova–dust interactions. We have also presented some of the latest-ever optical spectra for this type of supernova.

During the 300–795 day period, the SED of SN 2004et is best described in three parts: (1) a hot component due to emission from optically thick gas, as well as free–bound radiation; (2) a warm component due to newly formed, radioactively heated dust in the ejecta; and (3) a cold component due to an IR echo from the ISM dust of the host galaxy, NGC 6946. There may also have been a small contribution to the IR SED due to free–free emission from ionized gas in the ejecta. While it is conceivable that the warm component might alternatively have been caused by an IR echo from dust in the progenitor CSM, the fine-tuning required to make this scenario work, plus the blueshift in the [O I] λ6300 line after day 300 and the accelerated decline in the optical light curves, persuades us that a warm source in newly formed ejecta dust is more likely.

Our modeling of the warm component SED for the 300–795 day era demonstrates that the dust responsible for the MIR radiation must be made of silicate material. This is the first time that direct spectroscopic evidence has been presented for silicate dust formed in the ejecta of a recent supernova. Additional support for the silicate scenario comes from our detection of a large, but declining, mass of SiO, a key compound in the silicate-formation sequence. The mass of directly detected dust grew to no more than a few times 10^{-4} $M_\odot$.

A remarkable result of our analysis is that the model radius remained constant (standard deviation < 10%) throughout the 300–795 day era, yet the SN itself expanded by a factor of 2.65. We propose that this constitutes evidence that the dust formed in small, dense, comoving clumps, similar to the scenario argued for SN 1987A. Such clumps might arise in localized regions of density enhancement. With more efficient cooling in such regions, the clumps might be unable to expand against the hotter, higher pressure interclump gas. We investigated the case of a flat distribution of uniform-density clumps and showed that such a scenario could indeed account for the apparent constancy of the radius of the IR emission region. Moreover, we found that the derived dust masses are much the same as in the case of a uniform cloud of dust; the invocation of uniform-density clumps does not allow us to "hide" larger masses of dust.

We have shown that the cold residual component is well reproduced by a single IR-echo model, where the SN UV/optical flux is reradiated by the interstellar dust of NGC 6946. The model match plus the demand that the ISM number density should not exceed 1 cm^{-3} (assuming a dust/gas mass ratio of ~0.006) implies a dust-free cavity of radius 8–16 pc, possibly caused by the stellar winds of the progenitor and other nearby stars. While we assumed that the interstellar grains are made of amorphous carbon, we do not rule out other grain materials. The important point about our ISM IR-echo model is that with a single pair of input parameters (the dust-free cavity radius and the ISM dust density), we can account for the cold component throughout the 300–1395 day era. This gives us confidence that the ISM IR-echo interpretation is correct.

An interesting prediction from this result is that the echo luminosity should remain high for some decades. Moreover, the diameter of the echo annulus on the sky should increase to several arcseconds over the next ~10 yr, potentially resolvable by upcoming MIR space missions. We also note that the occurrence of such cold IR echoes should be relatively common for SNe occurring in dusty, late-type galaxies. Meikle et al. (2007) have already pointed out that such an echo provides a natural explanation for the cool MIR flux at days 670–681 from SN 2003gd.

After ~1000 days, we observed a remarkable rise in the optical and MIR fluxes. In addition, by day 823 the optical spectral lines had developed wide, box-shaped profiles with evidence of dust attenuation within the line-producing region. We interpret these results as being due to the impact of the ejecta

on the progenitor CSM, with the MIR flux rise and optical line attenuation resulting from dust formation within the cool dense shell. We estimate a CDS dust mass of (2–5) $\times 10^{-4}\ M_{\odot}$, a CDS radius of ∼6000 AU, and a total mass of 0.03–0.08 $M_{\odot}$. For a red supergiant wind, this mass is entirely plausible. Also, for a typical velocity of 10 km s^{-1}, the radius indicates a CSM age of ∼2700 yr.

The work presented here adds to the growing number of studies that do not support the contention that SNe are responsible for the large masses of dust in high-redshift galaxies. There may still be some possibility for the existence of large masses of undetected ejecta dust in young SNe. Such dust might (1) be formed after the end of the observations, (2) be hidden in nonuniform density distributions, or (3) exist at very low temperatures and so go undetected in MIR/FIR studies. But there are difficulties with each scenario. Option (1) would be in conflict with dust-condensation models (Todini & Ferrara 2001; Nozawa et al. 2003) which suggest that the bulk of the dust condensation is complete within two years past explosion. Our study, which includes the effects of clumping, reduces the plausibility of option (2). Possibility (3) requires most of the dust formed in the ejecta to rapidly cool to less than a few 100 K. It is not clear if this is physically possible, nor whether such a scenario could be made to be consistent with the optical depths indicated by the MIR spectra.

This study has demonstrated the rich, multifaceted ways in which a typical core-collapse supernova and its progenitor can produce and/or interact with cosmic dust. The range of distance scales over which we observe these processes is also noteworthy: typically 300 AU for the ejecta dust, 6000 AU for the CDS, and over 2 $\times 10^6$ AU for the IS IR echo. We have shown that, at least in the case of silicate dust, through the use of MIR spectra we can estimate total masses of dust even in uniform-density clumps that are optically thick *in the MIR*. We find that the mass of directly observed dust produced either in the ejecta or CDS never exceeded $10^{-3}\ M_{\odot}$. This is consistent with a steadily increasing number of similar results.

We thank R.M. Crockett and collaborators for their permission to use their optical observations of the SN 2004et field prior to publication. This work is based on observations made with the *Spitzer Space Telescope*, which is operated by the Jet Propulsion Laboratory, California Institute of Technology under a contract with NASA. Support for this work was provided by NASA through an award issued by JPL/Caltech. A.V.F. gratefully acknowledges additional support from NSF grant AST–0607485. J.S. is a Royal Swedish Academy of Sciences Research Fellow supported by a grant from the Knut and Alice Wallenberg Foundation. S.M. acknowledges support from the Academy of Finland (project 8120503). The Dark Cosmology Centre is funded by the Danish National Research Foundation. We thank the SUSPECT team for continued maintenance of their excellent database. Some of the data presented herein were obtained at the W.M. Keck Observatory, which is operated as a scientific partnership among the California Institute of Technology, the University of California, and NASA; it was made possible by the generous financial support of the W.M. Keck Foundation. We wish to extend special gratitude to those of Hawaiian ancestry on whose sacred mountain we are privileged to be guests. A.V.F. thanks the Aspen Center for Physics, where he participated in a workshop on Wide-Fast-Deep Surveys while this paper was nearing completion.

APPENDIX

INFRARED RADIATION FROM A CLOUD OF DUST CLUMPS

Consider a spherical "cloud" of uniform clumps, with a cloud radius of $R_{\rm cd}$. A clump-size distribution $dn_{\rm cl} = k_1 R_{\rm cl}^{-m_1} dR_{\rm cl}$ is invoked, where $dn_{\rm cl}$ is the number density of clumps having radius $R_{\rm cl} \rightarrow R_{\rm cl} + dR_{\rm cl}$ and k_1 is the clump number density scaling factor (i.e., it controls the total number of clumps in the cloud). At any given time, each clump has the same uniform number density of dust grains.

In the original IDM (Meikle et al. 2007), we can reexpress the luminosity equation as

$$L_{cl}(\nu) = 4\pi B(\nu, T)\sigma_{cl}(\nu), \tag{A1}$$

where the effective cross section of the dust sphere, $\sigma_{\rm cl}(\nu)$, is given by

$$\sigma_{\rm cl}(\nu) = \pi R_{\rm cl}^2(1 - e^{-\tau'_{\rm cl}(\nu)}) = \pi R_{\rm cl}^2[0.5\tau_{\rm cl}(\nu)^{-2}(2\tau_{\rm cl}(\nu)^2 - 1 + (2\tau_{\rm cl}(\nu) + 1)e^{-2\tau_{\rm cl}(\nu)}],$$

where $\tau'_{\rm cl}(\nu)$ is the effective optical depth of the dust sphere at frequency ν and $\tau_{\rm cl}(\nu)$ is the surface to center optical depth of the sphere at frequency ν. Now $\tau_{\rm cl}(\nu) = \gamma R_{\rm cl}$, where $\gamma = \frac{4}{3}\pi k\rho\kappa(\nu)\frac{1}{4-m}[a_{\rm (max)}^{4-m} - a_{\rm (min)}^{4-m}]$ and where ρ and $\kappa(\nu)$ are, respectively, the density and the mass absorption coefficient of the grain material (Meikle et al. 2007).

The luminosity of a single grain, $L_g(\nu)$, is given by $L_g(\nu) = 4\pi^2 a^2 Q(\nu)B(\nu, T)$. Using this to eliminate $4\pi B(\nu, T)$ from Equation (A1), we obtain

$$L_{\rm cl}(\nu) = L_g(\nu)\sigma_{\rm cl}(\nu)/(\pi a^2 Q(\nu)) = L_g(\nu)(\sigma_{\rm cl}(\nu)/\sigma_g(\nu)),$$

where $\sigma_g(\nu) = \pi a^2 Q(\nu)$ is the grain absorption cross section. By analogy, we can write for the cloud of clumps that

$$L_{\rm cd}(\nu) = L_{\rm cl}(\nu)(\sigma_{\rm cd}(\nu)/\sigma_{\rm cl}(\nu)) = L_g(\nu)(\sigma_{\rm cd}(\nu)/\sigma_g(\nu)), \tag{A2}$$

where

$$\sigma_{\rm cd}(\nu) = \pi R_{\rm cd}^2(1 - e^{-\tau'_{\rm cd}(\nu)}) = \pi R_{\rm cd}^2 \times [0.5\tau_{\rm cd}(\nu)^{-2}(2\tau_{\rm cd}(\nu)^2 - 1 + (2\tau_{\rm cd}(\nu) + 1)e^{-2\tau_{\rm cd}(\nu)}], \tag{A3}$$

$\tau'_{\rm cd}(\nu)$ is the effective optical depth of the cloud at frequency ν, and $\tau_{\rm cd}(\nu)$ is the surface to center optical depth of the cloud at frequency ν.

To determine $\tau_{\rm cd}(\nu)$, let us consider the case where the cloud contains a number of uniform-density clumps with a size distribution, $dn_{\rm cl} = k_1 R_{\rm cl}^{-m_1} dR_{\rm cl}$, as given above. Thus,

$$d\tau_{\rm cd}(\nu) = R_{\rm cd}\pi R_{\rm cl}^2(1 - e^{-\tau'_{\rm cl}(\nu)})k_1 R_{\rm cl}^{-m_1} dR_{\rm cl}.$$

Integrating from $R_{\rm cl(min)}$ to $R_{\rm cl(max)}$, we have

$$\begin{aligned}\tau_{\rm cd}(\nu) &= \pi R_{\rm cd}k_1 \int_{R_{\rm cl(min)}}^{R_{\rm cl(max)}} (1 - e^{-\tau'_{\rm cl}(\nu)})R_{\rm cl}^{2-m_1} dR_{\rm cl} \\ &= \pi R_{\rm cd}k_1 \int_{R_{\rm cl(min)}}^{R_{\rm cl(max)}} [0.5\tau_{\rm cl}(\nu)^{-2}(2\tau_{\rm cl}(\nu)^2 - 1 \\ &\quad + (2\tau_{\rm cl}(\nu) + 1)e^{-2\tau_{\rm cl}(\nu)}]R_{\rm cl}^{2-m_1} dR_{\rm cl} \\ &= \pi R_{\rm cd}k_1 \int_{R_{\rm cl(min)}}^{R_{\rm cl(max)}} \frac{1}{2\gamma^2}(2\gamma^2 R_{\rm cl}^2 - 1 \\ &\quad + (1 + 2\gamma R_{\rm cl})e^{-2\gamma R_{\rm cl}})r_{\rm cl}^{-m_1} dR_{\rm cl}.\end{aligned}$$

For the case where $m_1 = 0$ (i.e., a flat clump-size distribution), this integrates to

$$\tau_{\rm cd}(\nu) = \frac{1}{2\gamma^3}\pi R_{\rm cd} k_1 \times \left[\left(\frac{2}{3}\gamma^3 R_{\rm cl}^3 - \gamma(1+e^{-2\gamma R_{\rm cl}})R_{\rm cl} - e^{-2\gamma R_{\rm cl}}\right)\right]_{R_{\rm cl(min)}}^{R_{\rm cl(max)}}.$$

Substituting into Equation (A3), we obtain $\sigma_{\rm cd}(\nu)$. This can then be used to obtain $L_{\rm cd}(\nu)$ via Equation (A2). It may also be shown that the total mass of dust in the cloud when $m_1 = 0$ is given by

$$M_{\rm cd} = \frac{16}{27}\pi^3 R_{\rm cd}^3 \rho k k_1 \frac{1}{4-m}\left(a_{\rm (max)}^{4-m} - a_{\rm (min)}^{4-m}\right)\left(R_{\rm cl(max)}^4 - R_{\rm cl(min)}^4\right),$$

and the total number of dust clumps is

$$N_{\rm cl} = \frac{4\pi}{3(1-m_1)} R_{\rm cd}^3 k_1 (R_{\rm cl(max)} - R_{\rm cl(min)}).$$

REFERENCES

Alard, C. 2000, A&AS, 144, 363
Alard, C., & Lupton, R. H. 1998, ApJ, 503, 325
Barlow, M. J., et al. 2005, ApJ, 627, 113
Bertoldi, F., et al. 2003, A&A, 406, L55
Bianchi, S., & Schneider, R. 2007, MNRAS, 378, 973
Blair, W. P., Ghavamian, P., Long, K. S., Williams, B. J., Borkowski, K. J., Reynolds, S. P., & Sankrit, R. 2007, ApJ, 662, 998
Bode, M. F., & Evans, A. 1980, A&A, 89, 158
Bouchet, P., et al. 2006, ApJ, 650, 212
Cardelli, J. A., Clayton, G. C., & Mathis, J. S. 1989, ApJ, 345, 245
Cernuschi, F., Marsicano, F., & Codina, S. 1967, Annales d'Astrophysique, 30, 1039
Chevalier, R. A., & Fransson, C. 2003, in Supernovae and Gamma-Ray Bursters, ed. K. Weiler, Lecture Notes in Physics, vol. 598 (Berlin: Springer), 171
Chevalier, R. A., Fransson, C., & Nymark, T. K. 2006, ApJ, 641, 1029
Couch, S. M., et al. 2009, ApJ, 696, 953
Draper, P. W., et al. 2002, Starlink User Note, 214.10
Dunne, L., Eales, S., Ivison, R., Morgan, H., & Edmunds, M. 2003, Nature, 424, 285
Dunne, L., et al. 2009, MNRAS, 394, 1307
Dwek, E. 1983, ApJ, 274, 175
Dwek, E. 2004, ApJ, 607, 848
Dwek, E., Galliano, F., & Jones, A. P. 2007, ApJ, 662, 927
Elmhamdi, A., et al. 2003, MNRAS, 338, 939
Ercolano, B., Barlow, M. J., & Sugerman, B. E. 2007, MNRAS, 375, 753
Faber, S. M., et al. 2003, SPIE, 4841, 1657
Fesen, R. A., et al. 2001, ApJS, 133, 161
Filippenko, A. V. 1982, PASP, 94, 715
Filippenko, A. V., et al. 2004, IAU Circ., 8414
Fransson, C., et al. 2005, ApJ, 622, 991
Gerardy, C. L., et al. 2000, ApJ, 607, 391
Gomez, H. L., et al. 2009, MNRAS, 397, 1621
Graham, J. R., & Meikle, W.P.S. 1986, MNRAS, 221, 789
Hachisu, I., et al. 1991, ApJ, 368, 27
Hamuy, M. 2003, AJ, 582, 905
Hashimoto, M., Nomoto, K., & Shigeyama, T. 1989, A&A, 210, L5
Herant, M., & Woosley, S. E. 1994, ApJ, 425, 814
Hines, D. C., et al. 2004, ApJS, 154, 290
Houck, J. R., et al. 2004, ApJS, 154, 18
Hoyle, F., & Wickramasinghe, N. C. 1970, Nature, 226, 62
Karachentsev, I. D., Sharina, M. E., & Huchtmeier, W. K. 2000, A&A, 362, 544
Kifonidis, K., et al. 2006, A&A, 453, 661
Kotak, R., et al. 2005, ApJ, 628, L123
Kotak, R., et al. 2006, ApJ, 651, L117
Kozasa, T., et al. 1989, ApJ, 344, 325
Krause, O., Birkmann, S. M., Rieke, G. H., Lemke, D., Klaas, U., Hines, D. C., & Gordon, K. D. 2004, Nature, 432, 596
Laor, A., & Draine, B. T. 1993, ApJ, 401, 441
Leonard, D. C., et al. 2000, ApJ, 536, 239
Li, H., McCray, R., & Sunyaev, R. A. 1993, ApJ, 419, 824
Li, W., Van Dyk, S. D., Filippenko, A. V., & Cuillandre, J.-C. 2005, PASP, 117, L121
Liu, W., & Dalgarno, A. 1994, ApJ, 428, 769
Lucy, L. B., et al. 1989, Lecture Notes in Physics Vol. 350, ed. G. Tenorio-Tagle, M. Moles, & J. Melnick (Berlin: Springer), 164
Lucy, L. B., et al. 1991, in Supernovae, ed. S. E. Woosley (New York: Springer), 82
Martí-Vidal, I., et al. 2007, A&A, 470, 1071
Matheson, T., Filippenko, A. V., Ho, L. C., Barth, A. J., & Leonard, D. C. 2000, AJ, 120, 1499
Mathis, J. S., et al. 1977, ApJ, 217, 425
Mattila, S., et al. 2008, MNRAS, 389, 141
Meikle, W. P. S., et al. 2006, ApJ, 649, 332
Meikle, W. P. S., et al. 2007, ApJ, 665, 608
Misra, K., et al. 2007, MNRAS, 381, 280
Morgan, H. L., & Edmunds, M. G. 2003, MNRAS, 343, 427
Nomoto, K., Shigeyama, T., Kumagai, S., & Yamaoka, H. 1991, in Supernovae, ed. S. E. Woosley (New York: Springer), 176
Nozawa, T., Kozasa, T., Umeda, H., Maeda, K., & Nomoto, K. 2003, ApJ, 598, 78
Nozawa, T., et al. 2007, ApJ, 666, 955
Oke, J. B., et al. 1995, PASP, 107, 375
Osterbrock, D. E. 1989, Astrophysics of Gaseous Nebulae and Active Galactic Nuclei (Mill Valley, CA: Univ. Science Books)
Pei, Y. C., Fall, S. M., & Bechtold, J. 1991, ApJ, 378, 6
Pettini, M., et al. 1997, ApJ, 478, 536
Pozzo, M., et al. 2004, MNRAS, 352, 457
Rho, J., Jarrett, T. H., Chugai, N. N., & Chevalier, R. A. 2007, ApJ, 666, 1108
Rho, J., Jarrett, T. H., Reach, W. T., Gomez, H., & Andersen, M. 2009, ApJ, 693, L39
Rho, J., et al. 2008, ApJ, 673, 271
Roche, P., Aitken, D., & Smith, C. 1991, MNRAS, 252, 39
Rouleau, F., & Martin, P. G. 1991, ApJ, 377, 526
Sahu, D. K., Anupama, G. C., Srividya, S., & Muneer, S. 2006, MNRAS, 372, 1315
Sandstrom, K. M., Bolatto, A. D., Stanimirovic, S., van Loon, J. Th., & Smith, J. D. T. 2009, ApJ, 696, 2138
Smith, N., et al. 2008, ApJ, 680, 568
Stanimirovic, S., Bolatto, A. D., Sandstrom, K., Leroy, A. K., Simon, J. D., Gaensler, B. M., Shah, R. Y., & Jackson, J. M. 2005, ApJ, 632, L103
Stockdale, C. J., et al. 2004, IAU Circ., 8415
Sugerman, B. E. K., et al. 2006, Science, 313, 196
Temim, T., et al. 2006, AJ, 132, 1610
Todini, P., & Ferrara, A. 2001, MNRAS, 325, 726
Wade, R. A., & Horne, K. D. 1988, ApJ, 324, 411
Werner, M. W., et al. 2004, ApJS, 154, 1
Williams, B.J., et al. 2006, ApJ, 652, L33
Wooden, D., et al. 1993, ApJS, 88, 477
Woosley, S. E., & Weaver, T. A. 1995, ApJS, 101, 181
Wright, E. L. 1980, ApJ, 242, L23
Zwitter, T., & Munari, U. 2004, Central Bureau Electronic Telegrams, 95, 1
Zwitter, T., Munari, U., & Moretti, S. 2004, IAU Circ., 8413